FAKULTÄT FÜR PHYSIK
Physikalisches Institut
DEPARTMENT OF APPLIED PHYSICS
Nanospin Group

Active Control of Spin Waves in Micro- and Nanoscale YIG-based Magnetic Structures

Final Project
by

Felix Hermann

Reviewer:	Prof. Dr. W. Wulfhekel
Second Reviewer:	Priv-Doz. Dr. K. Zakeri
External Reviewer:	Prof. Dr. S. van Dijken
Advisor:	Dr. H. Qin

Acknowledgments

I want to thank Piv.-Doz. Dr. Khalil Zakeri for offering me this opportunity, Prof. Dr. Wulfhekel for helping with bureaucratic hurdles and Dr. Huajun Qin and Prof. Dr. Sebastiaan van Dijken for excellent supervision during my whole stay in Finland with all matters. Thanks for letting me gain experience and knowledge in all kinds of research work, from sample growth to fabrication in cleanroom, from measurement and characterization to analysis and writing. In addition, I want to thank Dr. Rasmus Holländer for discussions on my thesis and all the answers on my sudden physics questions, even if it was on a Saturday evening.

Minä haluan sanoa ”Kiitos paljon” Fyysikkokillalle, että minä sain tutustua Teekarikulttuuriin, moniin hauskoihin ja kivoihin ihmisiin, juhlia, saunoa ja käydä sitseillä.

Herewith, I declare that this thesis is composed by myself. Thus, I did not use other than the noted sources and resources. All directly or indirectly quoted material is marked as such. Furthermore, I took notice of the "Satzung des KIT zur Sicherung guter wissenschaftlicher Praxis".

Karlsruhe, the 27.03.2020, 

Felix Hermann

Karlsruhe, the 27.03.2020,

Prof. Dr. W. Wulfhekel

Abstract

Magnonic devices based on active manipulation of spin waves, provide a broad set of solutions to many problems in CMOS technology as these can be operated at very high switch speeds on nanoscale while only very low thermal losses are experienced. Therefore, this work aims to utilize one–dimensional magnonic crystals and resonators that promise new routes towards nanoscale devices.
In this work growth of ultra low damping nanometer thin YIG films by Pulsed Laser Deposition, patterning by means of optical and electron beam lithography, sputtering and ion beam etching as well as characterization of these devices by all-electric broadband spin wave spectroscopy are explained. By etching several magnonic crystals in 43 nm thick YIG deep and wide bandgaps are opened by Bragg Scattering. These magnonic crystals consist of several shallow air grooves with varying lattice period, groove width and groove depth. By optimizing crystal parameters, the bandgaps suppress spin-wave transmission down to background while transmission for allowed frequencies is comparable to continuous YIG. With a total size of less than 10 µm this is the smallest YIG magnonic crystal compared to literature.
By developing a second approach utilizing narrow magnonic resonators consiting of CoFeB grown on top of continuous YIG film, damaging magnetic properties in YIG induced by air groove fabrication is avoided. Within that bilayer, the YIG spin-wave undergoes a asymmetric wavelength down shift. Superposition of reflected waves from the resonator edges leads to destructive interference for well-defined frequencies. This enables robust, deep and wide bandgaps with a resonator width as narrow as 250 nm, while keeping transmission in off-resonance frequencies unaffected.

The results provided in this work offer promising prospects for engineering broad and deep bandgap in a large frequency range on the micro- and nanometer scale. Herewith, a big step towards highly efficient nanoscale YIG magnonics is achieved.

Zusammenfassung

Magnonische Geräte auf Basis aktiver Spin-Wellen-Manipulation bieten eine Bandbreite an Lösungen zu vielen Problemen der CMOS-Technologie, da diese mit hohen Schaltgeschwindigkeiten auf Nanoskala betrieben werden können, während gleichzeitig nur niedrige Hitzeverluste auftreten. Darum zielt diese Arbeit darauf ab, ein-dimensionale magnonische Kristalle und Resonatoren zu benutzen, welche einen neuen Weg zu nanoskaligen Geräten versprechen.
In dieser Arbeit sind YIG-Filme mit ultraniedrigen magnetischen Dämpfungseigenschaften gewachsen durch "Pulsed Laser Deposition" sowie strukturiert mit Hilfe von optischer und Elektronenstrahl-Lithographie, Sputtern und Ionenstrahl-Ätzen. Weiter ist die Charakterisierung dieser Geräte durch Rein-Elektrische Breitband-Spin-Wellen-Spektroskopie erklärt. Durch das Ätzen einiger Magnonischer Kristalle in 43 nm dickem YIG-Film sind tiefe und breite Bandlücken mit Hilfe von Bragg-Streuung eröffnet. Diese magnonischen Kristalle bestehen aus mehreren Luftrillen mit variierender Gitterperiode, Rillenbreite und Rillentiefe. Durch Optimieren der Kristall-Parameter wird die Spin-Wellen Transmission in Bandlücken bis zum Hintergrundniveau unterdrückt, während Transmission für erlaubte Frequenzen vergleichbar zu kontinuierlichem YIG bleibt. Mit einer Gesamtbreite von weniger als 10 µm ist dies der kleinste magnonische YIG-Kristall in vergleichbarer Literatur.
Durch Entwickeln eines zweiten Ansatzes, bei dem aufgewachsene schmale magnonische Resonatoren aus CoFeB auf dem kontinuierlichen YIG-Film verwendet werden, kann der durch Fabrikation von magnonischen Luftrillen-Kristallen eingebrachte Schaden an den magnetischen Eigenschaften des YIGs vermieden werden. Innerhalb dieser Doppelschicht unterliegt die Spin-Welle einer asymmetrischen Wellenlängenschrumpfung. Superposition von an den Resonatorkanten reflektierten Wellen führt zu destruktiver Interferenz für wohl-definierte Frequenzen. Dies ermöglicht robuste, tiefe und breite Bandlücken mit einer Resonatorbreite von lediglich 250 nm, während gleichzeitig Transmission von nicht-resonante Frequenzen unverändert bleiben.

Die Ergebnisse dieser Arbeit bieten eine vielversprechende Perspektive um breite und tiefe Bandlücken in einem breiten Frequenzspektrum auf der Mikro- und Nanometerskala zu konstruieren. Damit ist ein großer Schritt in Richtung hoch-effizienter nanoskaliger YIG-Magnonik erreicht.

Contents

List of Acronyms and Abbreviations ix

Introduction 1

1 Theoretical Background 3
1.1 Magnetism and Magnetization Dynamics . . . 3
1.1.1 Micromagnetic Interactions . . . 3
1.1.2 Magnetization Dynamics and Landau-Lifshitz-Gilbert Equation . . . 5
1.2 Spin-Waves . . . 6
1.3 Active Magnonic Media . . . 9

2 Methods 11
2.1 Sample Preparation . . . 11
2.2 Device Fabrication . . . 15
2.3 Broadband spin-wave Spectroscopy . . . 19

3 Results and Discussion 23
3.1 Air Groove–based Magnonic Crystals . . . 23
3.1.1 Comparison of air groove MC to bare YIG . . . 25
3.1.2 Variation of various Device Parameters . . . 26
3.2 YIG-Based Magnonic Resonators . . . 31
3.2.1 Dispersion of Spin-Waves in a YIG CoFeB Bilayer . . . 33
3.2.2 Nanoscale Magnonic Resonators . . . 38

4 Conclusion and Outlook 41

Bibliography 43

Index 45

List of Figures

1.1 Damped precession of a magnetic moment in an external magnetic bias field . . . 6
1.2 spin-wave Dispersions for different geometries . . . 8

2.1 PLD-Setup . . . 12
2.2 Thin film growth . . . 13
2.3 Dependence of the FMR frequency and FWHM of the FMR peak on magnetic bias field . . . 14
2.4 Schematics of the structures . . . 16
2.5 Schematic of the device fabrication steps . . . 17
2.6 AFM images of 50 nm-thick CoFeB stripes on top of a continuous YIG film . . . 18
2.7 Broadband spin-wave spectroscopy measurement setup . . . 20
2.8 Schematic of microwave antennas and contact pads . . . 21

3.1 Contour plots of spin-wave transmission spectra of $a2w0.5N4$ MC . . . 24

3.2 Position of the bandgap frequency and width as a function of magnetic fields . . 25
3.3 spin-wave transmission spectra of $a2w0.5N4$ MC compared to bare YIG 26
3.4 Gap tuning as a function of periodicity 28
3.5 Gap tuning as a function of width 29
3.6 spin-wave transmission spectra for MCs with different air groove depth 30
3.7 spin-wave Transmission contour plots for magnonic resonator arrays and single stripe 32
3.8 Comparison of array and single stripe CoFeB devices 32
3.9 Schematic of the bilayer 33
3.10 Dispersion relations for YIG spin-waves in CoFeB-YIG bilayer 35
3.11 Reflection and Transmission in a magnonic resonator device 35
3.12 Spin-wave transmission spectra of various single magnonic resonators 39
3.13 Prediction, position of the bandgap frequency, and bandgap width as a function of magnetic field and magnonic resonator width 40

List of Tables

2.1 Summary of experimentally derived parameters of the samples 14
2.2 Parameters used in the fabrication of resist layers 15

3.1 Summary of parameters for the first band gaps in Figure 3.5 27

List of Acronyms and Abbreviations

AFM Atomic Force Microscopy

AZ351B A developer used for direct laser writing lithography

AZ5214E A photoresist used for direct laser writing lithography

CoFeB Cobalt Iron Boron alloy

CPW Coplanar Waveguide

FMR Ferromagnetic Resonance

GGG Gadolinium Gallium Garnet, chemical formula $Gd_3Ga_5O_{12}$

GSG Ground-Source-Ground, a type of three point probes with two ground lines surrounding one source line.

LLG Landau-Lifshitz-Gilbert-Equation

MC Magnonic Crystal

MIBK A developer used for electron-beam lithography

PLD Pulsed Laser Deposition

PMMA A4 A resist used for electron-beam lithography

VNA Vector Network Analyzer, a multiport device for high-frequency electric signal handling

YIG Yttrium Iron Garnet, chemical formula $Y_3Fe_2(FeO_4)_3$

Introduction

High processing capabilities of modern computers are important for all kinds of research and daily life. Due to increasing demand and use of computing in big data analysis, life imaging, video processing technologies and complex simulations, the necessary power rises. However, within the past 10 years CMOS technology got close to its physical limit in miniaturization and cooling capacities. Hence, a new widely usable, flexible and fast information processing technology is needed. [Schaller, 1997], [Serga et al., 2010] While electronics utilizes charge of electrons, magnonics utilizes the amplitude and phase information of spin waves. By providing fast group velocities, a broad frequency range, and low Joule heating, they could serve as excellent information carriers and transmitters. Parallel computing within one device could be realized, and thus the processing speed multiplies. [Krawczyk and Grundler, 2014], [Khitun, 2012]

A promising material for magnonics is *y*ttrium *i*ron *g*arnet (YIG), since it exhibits ultra low magnetic damping. However, high quality thin film growth and device fabrication on the nanoscale are big challenges, even with today's lithography and growth techniques. [Serga et al., 2010], [Neusser and Grundler, 2009]
This work aims to tackle the named problems by growing nanometer thick YIG films with ultra low intrinsic Gilbert damping and fabricating a sub-10 µm magnonic crystals for control of spin-wave in Damon Eshbach geometry. This magnonic crystals consists of periodic air groove arrays that are fabricated by means of electron beam lithography and ion beam etching. By varying MC parameters such as lattice period, groove width, and magnetic bias field, the bandgaps opened up by Bragg scattering are flexibly designed and actively manipulated.
Bragg scattering of propagating spin-waves in these crystals opens up forbidden frequency gaps when their wavelength (λ) matches $\lambda = \frac{2a}{n}$ (lattice period a, integer n) Thus, the minimal size of a magnonic crystals exceeds the wave length of the propagating spin-wave it aims to manipulate. In addition, the ion milling deteriorates the YIG film at the edges, challenging further downscaling to nanometer range. To address this challenge, a new concept for YIG-based magnonic resonators is introduced. By utilizing a bilayer of CoFeB and continuous YIG, wide bandgaps are opened in the spin wave transmission spectrum. To understand the mechanism for opening transmission bandgaps by the bilayer region, the model for magnetostatic dispersion by [Grünberg, 1981] is extended to the dipolar-exchange-regime. The incident magnetostatic spin-wave in bare YIG converts in the bilayer region, respecting a fundamentally altered and asymmetrical dispersion. Resonant reflection at the device edges lead to interference of waves at the detecting antenna. For positive wavevector, the spin wave converts to the dipolar exchange regime and short wavelengths. From the model it follows, that the necessary phase delay for destructive interference is already obtained by a single 250 nm wide stripe. A detailed investigation of transmission bandgaps relating to stripe width is conducted. Thus, control of bandgap spin wave transmission on the nanoscale is obtained.
These outcomes may lead to the implementation and improvement of devices for nanoscale information processing.

1. Theoretical Background

Magnetism is a field closely related to electricity and yet very different. Electronic properties in solids as, e.g., dispersion, can be mainly explained by one-electron-approximation. However, this is not true for magnetism. To model the many facettes of magnetism, aspects of multiple energy contributions have to be compared and evaluated. [Ibach and Lüth, 2002]
Thus, the following chapter will give a short review on important energy interactions, dynamics and eventually spin waves and magnonic crystals. For further reading and detailed discussions and derivations, e.g., [Stancil, 1993], [Stancil and Prabhakar, 2009] and [Aharoni et al., 2000] are recommended.

The most important material in this work is YIG. It is an oxide material with ferrimagnetic properties and a Curie-temperature of $T_C = 559\,K$. YIG exhibits ultralow magnetic damping and it is also used in electronics as it has a very high *quality-factor* for microwave applications. [Cherepanov et al., 1993]

1.1 Magnetism and Magnetization Dynamics

As described in [Ibach and Lüth, 2002] macroscopic magnetism is categorized in 5 different types, namely ferromagnetism, paramagnetism, diamagnetism, ferrimagnetism and antiferromagnetism. These types originate in different outcome of superposition of energies which can be derived from mean-field-approximations and next-neighbor-approximations. In the following four important energies resulting from microscopic interactions are introduced.

1.1.1 Micromagnetic Interactions

The total energy E_{tot} of micromagnetic systems consists of different energy contributions. A magnetic field can be assigned, which holds $H_{eff} = \sum_i H_i$. H_i describes the magnetic contributions of the different energy terms. In this work, the main contributions are the magnetic anisotropy, the Zeeman energy, the exchange interaction and the magnetostatic contribution. These contributions are discussed in detail in [Daniel D. Stancil, 2009] and [Stancil, 1993].

Magnetic Anisotropy

Reduced neighbor symmetry in the lattice order at the surface deformes the electron orbitals. This then leads via spin-orbit coupling and coupling to the magnetic moment to a magnetic anisotropy. The field and its energy are described by: [Bilzer, 2007], [Hubert and Schäfer, 2008]

$$\begin{aligned} \vec{H}_{aniso} &= -\frac{1}{\mu_0}\vec{\nabla}_M E_{aniso} \\ E_{aniso} &= -\frac{k}{d}m_z^2 \end{aligned} \tag{1.1}$$

k is a material parameter. Other contributions like bulk anisotropy or uniaxial anisotropy are neglected.

Zeeman Contribution

When an external magnetic field $B_{ext.}$ is applied, magnetic moments μ_i in that field feel a torque. Thus, the magnetic moments align to the external field. The energy for this mechanism is lowest, when the magnetic field and magnetic moments align parallel. The Zeeman energy can be written as: [Stancil and Prabhakar, 2009]

$$E_{Zeeman} = -\mu_i \cdot B_{ext.} \tag{1.2}$$

Exchange Interaction

Following the approach of [Heitler and London, 1927] in [Stancil and Prabhakar, 2009], an energy eigenvalue is found from the Hydrogen molecule problem with 2 electrons When introducing the electrons as independent particles with orthogonal wave functions, the Heisenberg hamiltonian can be written as:

$$\mathcal{H}_{Heisenberg} = -\frac{2J_{12}}{\hbar^2} \cdot \vec{S}_1 \vec{S}_2 \tag{1.3}$$

Here, J is the exchange integral and describes the nature of interaction. $\vec{S}_i$ refers to the spin of electron i. In [Stancil and Prabhakar, 2009] the exchange integral is derived:

$$J = e^2 \cdot \int\int \Phi_a^*(\vec{r}_1)\Phi_b^*(\vec{r}_2) \left(\frac{1}{R_{ab}} + \frac{1}{r_{12}} - \frac{1}{r_{a1}} - \frac{1}{r_{b2}}\right) \Phi_b(\vec{r}_1)\Phi_a(\vec{r}_2)\, d^3r_1\, d^3r_2 \tag{1.4}$$

e describes the charge of the electrons 1 and 2, while R_{ab} the distance of atom a and b describes. r_{a1} etc. describes the distance of electrons to atoms or electrons, respectively. Here, the overlap of two atom wave functions Φ_a and Φ_b for the electrons 1 and 2 is integrated. This expresses Pauli's principle and coulomb repulsion.

By aligning the spins of electrons a magnetic order is provided. For positive solution of the integral, the parallel alignment leads to net magnetization and is called ferromagnetism. A negative solution and antiparallel alignment leads to the related antiferromagnetism without net magnetization. Ferrimagnetism is an antiparallel order that has different magnitude in one direction than the other.
Following a semi-classical ansatz, the exchange interaction energy is obtained from the quantum mechanical Heisenberg model by summing up the spin-spin interaction of neighbors j: (for full derivation, see [Aharoni et al., 2000])

$$E_i = -J_{ij} \cdot S \cdot \sum_j \cos\phi_{ij} \tag{1.5}$$

Here, J_{ij} describes the exchange integral of spin i and j. S is the sum of the spins and ϕ the angle between the spins. Since the spins align either positive or negative in a ferro- and antiferromagnets, a small-angle-approximation can be performed, which leads to:

$$E_i \approx J_{ij} \cdot S \cdot \sum_j \phi_{ij}^2 \tag{1.6}$$

Furthermore, it holds:

$$\sum_j \phi_{ij}^2 \underbrace{\approx}_{\text{small angle}} \left|\hat{m}_i - \hat{m}_j\right|^2 \tag{1.7}$$

Here, $\hat{m}_i$ corresponds to the unit vector along the spin and hence magnetic momentum. When introducing $s_i \nabla \vec{m} = m_i$, and transfer the summation in an integral, one obtains:

$$E_{Exchange} = A\left((\nabla m_x)^2 + (\nabla m_y)^2 + (\nabla m_z)^2\right) \tag{1.8}$$

The energies derived from this expression are one of the largest in magnetism. However, due to the very limited reach of spin-spin-neighbor interaction, exchange interaction is short-range in nature.

Magnetostatic Contribution

If a magnetized volume has physical boundaries, then these boundaries induce magnetic flux in and around the volume. All magnetic moments then perceive this flux. Following [Bilzer, 2007] and [Hubert and Schäfer, 2008], the energy can be derived solely from Maxwell's equations in magnetostatic approximation.

$$\begin{aligned} \vec{\nabla}\vec{B} = \mu_0 \cdot \vec{\nabla}\left(\vec{H}_{ms} + \vec{M}\right) = 0 \\ \Rightarrow \vec{\nabla}\vec{H}_{ms} = -\vec{\nabla}\vec{M} \end{aligned} \tag{1.9}$$

Here, $\vec{B}$ describes the magnetic flux, the magnetostatic field is $\vec{H}_{ms}$ and the magnetization refers to $\vec{M}$ Since, there is no current in this system, the rotation of the induced H-field must be zero:

$$\vec{\nabla} \times \vec{H}_{ms} = 0 \tag{1.10}$$

By introducing a magnetic potential Ψ_{mag} with magnetic density $\rho_{mag} = \Delta\Psi_{mag}$ and $-\vec{\nabla}\Psi_{mag} = \vec{H}_{ms}$, it follows:

$$\nabla\vec{H}_{ms} = \rho_{mag} = -\nabla\vec{M} \tag{1.11}$$

Since, the non-current induced magnetic flux lowers the magnetization it is also known as demagnetizing field. However, it is very difficult to calculate analytical solutions for the flux and these fields. The magnetostatic energy is described as: [Hubert and Schäfer, 2008]

$$E_{ms} = -\frac{\mu_0}{2V}\int_{sample} dV\vec{M} \cdot \vec{H}_{ms} \tag{1.12}$$

Here, V is the volume of the flux creating structure.

1.1.2 Magnetization Dynamics and Landau-Lifshitz-Gilbert Equation

The single most important equation to derive any modeling of dynamic microscale magnetic systems is the Landau-Lifshitz-Gilbert Equation, short LLG. When observing a system of spins, one can describe the time dependent evolution of magnetization vector $\vec{M}$ by the Landau-Lifshitz equation (LLE):

$$\frac{d\vec{M}}{dt} = \gamma\mu_0\vec{M} \times \vec{H_{eff}} \tag{1.13}$$

The effective magnetic field $\vec{H_{eff}}$ represents all contributions like external field, anisotropy or demagnetzing fields. From phenomenological interpretation of equation 1.13, it follows, that nonparallel magnetization $\vec{M}$ will feel a torque, which aligns it to the external field $\vec{H_{eff}}$. However, if in addition a radial movement of the magnetization exists, the result would be an endless precession, because no damping is included. [Stancil and Prabhakar, 2009] To include damping in

a large validity range, [Gilbert and Ekstein, 1956] extended that formula by including an intrinsic damping parameter α.

$$\frac{\mathrm{d}\vec{\mathrm{M}}}{\mathrm{dt}} = \gamma\mu_0\vec{\mathrm{M}} \times \vec{\mathrm{H}_{\mathrm{eff}}} + \frac{\alpha}{\mathrm{M_S}} \cdot \left(\vec{\mathrm{M}} \times \frac{\mathrm{d}\vec{\mathrm{M}}}{\mathrm{dt}}\right) \tag{1.14}$$

α corresponds here to an empiric material constant. The smaller this parameter, the longer the decay time. In Figure 1.1, this phenomenon is depicted. YIG is the material with the lowest Gilbert damping constants. Metals and alloys have much larger damping, but also much higher group velocities due to higher saturation magnetization. This makes them favorable in other approaches. [Serga et al., 2010]

Solving the LLG equation is often accomplished by using simulation software like *MuMax3* [Vansteenkiste et al., 2014]. There, the differential equation for the magnetization vector is solved locally by using massive amounts of computing power.

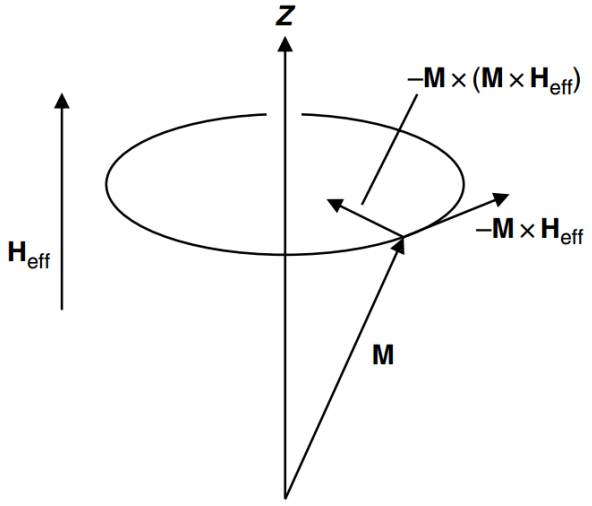

Reprinted from [Stancil and Prabhakar, 2009]

Figure 1.1: Damped precession of a magnetic moment in an external magnetic bias field.

1.2 Spin-Waves

When combining both, the LLG and spin interactions a description for collective spin precessions are obtained. Those are called spin-waves. The quasi particle of a spin-wave, is called *Magnon*. Phenomenologically, this is explained by an excitation transferred from one to another electron spin in a magnetically ordered material. This excitation will then propagate with a wave length λ, a frequency f and group velocity ν_{group}. The most often excitation techniques utilize a current that induces a small, local torque on spins, that excites them to precess. For detecting spin-waves, most often a second antenna or lasers are used. [Serga et al., 2010]

Ferromagnetic Resonance

In the used thin films in this work, an external magnetic bias field aligns all spins in one direction. The result is an uniformly magnetized film with $\vec{\mathrm{M}}_0 \parallel \vec{\mathrm{H}}_0$. A uniform spin precession is called ferromagnetic resonance (FMR). For this frequency $\mathrm{f_{FMR}}$, the spins precess in phase over very

long scale. This is described by the Kittel-formula. [Stancil and Prabhakar, 2009] To get a mathematical expression, a full derivation is concluded in [Kittel, 1948].

$$f_{FMR} = \frac{\gamma}{2\pi}\mu_0 \cdot \sqrt{H_{eff} \cdot (H_{eff} + M_{eff})} \tag{1.17}$$

H_{eff} describes the sum of magnetic contributions and M_{eff} is the effective magnetization. The gyromagnetic ratio $\frac{\gamma}{2\pi} = 28\,025\,\frac{MHz}{mT}$.

Since this formula describes the *resonant* behavior of the thin film, the expected results equates a lorentz shaped peak. From sweeping the magnetic field and fitting the FMR peak location to equation 1.17, the magnetization and anisotropy can be determined experimentally.

From analyzing the linear regression of FWHM by:

$$\mathrm{FWHM}\,(f_{FMR}) = 2\alpha f_{FMR} + \Delta k \nu_{group} \tag{1.15}$$

the intrinsic Gilbert damping parameter α can also be determined. $\Delta k \nu_{group}$ relates to the excitation spectrum line width of the antenna and spin-wave group velocity in the thin film.

Besides FMR, propagating spin-wave modes can also be excited in the magnetic films by local microwave excitation. Depending on the propagation direction and the orientation of the external magnetic bias field, there are three types of magnetostatic spin-waves, which will be explained in the following. Other excitations like purely exchange spin-waves are not the topic of this thesis. Although called magnetostatic, the waves are dynamic, but derived from Maxwell's Equations in magnetostatic approximation. [Serga et al., 2010]

Magnetostatic Surface Spin-Waves

In this work, only spin-waves in Damon Eshbach geometry ([Damon and Eshbach, 1961]) are investigated. The external magnetic bias field is aligned in plane and perpendicular to the propagation direction. The dispersion is plotted in Figure 1.2 (indicated by MSSW) A derivation to obtain the dispersion is computed in [Stancil, 1993]. There, the dispersion is found as:

$$f(k) = \frac{\gamma}{2\pi} \cdot \sqrt{H_{eff} \cdot (H_{eff} + \mu_0 M_{eff}) + \frac{(\mu_0 M_{eff})^2}{4} \cdot (1 - e^{-2kd})} \tag{1.16}$$

Here, the effective field is described by H_{eff} and the effective magnetization by M_{eff}. In the limit of $k \to 0$, the Kittel-Formula can be obtained:

$$f_{res} = f(k = 0) = \frac{\gamma}{2\pi} \cdot \sqrt{H_{eff} \cdot (H_{eff} + \mu_0 M_{eff})} \tag{1.17}$$

In [Wong et al., 2014], the localization of spin-wave in Damon Eshbach geometry is investigated. It is found, that for thick films, the wave is pinned to one surface $\vec{n} = \vec{H_0} \times \vec{k}$. However, due to leakage in thin films the amplitude ratio $\frac{A_{+y}}{B_{-y}}$ in opposite directions at the other surface is found as:

$$\frac{A_{+y}}{B_{-y}} > 2e^{|k_y|d} - e^{-|k_y|d} \tag{1.18}$$

Here, the thickness of the film corresponds to d and the wavenumber to k_y. The localization of spin-waves in the Damon Eshbach geometry at the surface and the out-of-plane component of the precession $\vec{m}(t)$ also allow for other observation techniques such as by Magneto-optical Kerr-Microscopy or Brilloiun Light Scattering. [Serga et al., 2010]

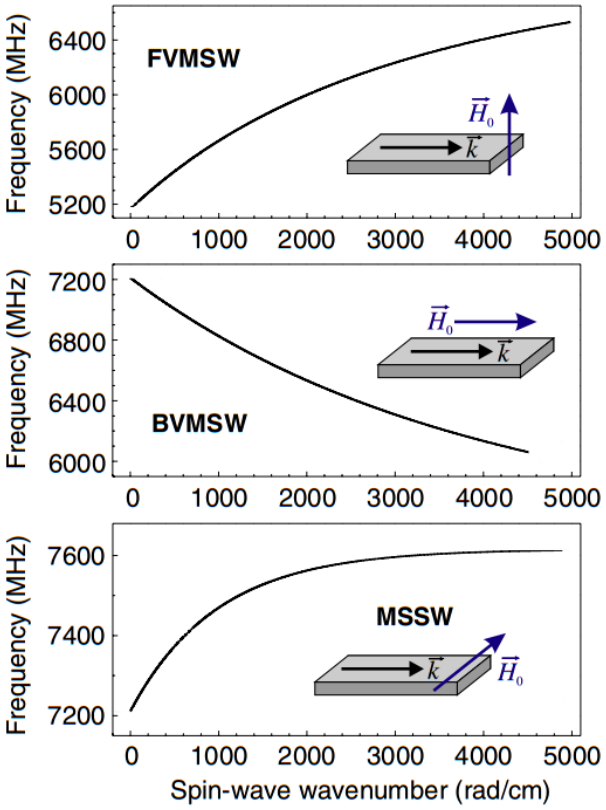

Reprinted from [Serga et al., 2010]

Figure 1.2: spin-wave Dispersions for different geometries. Each geometry is sketched in a small inset. The dispersions are calculated for a 5 µm thick YIG film with saturation magnetization $M_S = 175\,\frac{kA}{m}$ and an external applied magnetic bias field of $H_{Ext} = 185\,mT$.

Backward Volume Magnetostatic Spin Waves

Another way of aligning the magnetic bias field is in plane, but parallel to the spin-wave propagation direction. This configuration is called the Backward Volume mode, because the spin-wave follows a cosinusoidal distribution across the whole cross section of the film. In addition, the dispersion provides negative group velocities, i.e., the amplitude moves in the opposite direction than the energy transfer. [Serga et al., 2010] Thus, the highest frequency in this excitation mechanism is the FMR frequency. In Figure 1.2, the dispersion is shown which is described by: [Stancil, 1993]

$$f_{BVSW} = \sqrt{f_{res} \cdot \left(f_{res} + f_M \cdot \frac{1 - e^{-kd}}{kd} \right)} \quad \text{with } f_M = \frac{\gamma}{\mu_0} M_{eff} \text{ and Eq. 1.17} \tag{1.19}$$

Forward Volume Magnetostatic Spin Waves

A third configuration can be obtained by applying the bias field out of plane and perpendicular to spin-wave propagation. This case corresponds to slower group velocities than Damon Eshbach geometry as the dispersion is flatter.[Serga et al., 2010] The shown dispersion is computed from: [Stancil, 1993]

$$f_{FVSW} = \sqrt{f_H \cdot \left(f_H + f_M \cdot \left(1 - \frac{1 - e^{-kd}}{kd} \right) \right)} \quad \text{with } f_H = \frac{\gamma}{\mu_0} H_{ext} \tag{1.20}$$

A big advantage for application in this form is, that the magnetic field is always perpendicular to the propagation, even if the spin-wave changes direction in the film plane.

1.3 Active Magnonic Media

Similar to the electromagnetic waves in metal conductors, spin-waves can be manipulated by active media. This results in a band structure that changes upon external actuation depending on the nature of manipulator.

Magnonic Crystals

Spin-waves can be reflected on periodic magnetic elements similar to Bloch waves in solids at the unit cell borders. This can be realized by physical patterning magnetic films and thereby periodically manipulate the magnetic properties. For magnonic crystals, the reflection of propagating spin-waves is described by the Bragg scattering condition: [Serga et al., 2010]

$$\mathrm{k_{scatter}} = \frac{\mathrm{n} \cdot \pi}{\mathrm{a_0} \cdot \sin\theta} = \left.\frac{\mathrm{n}\pi}{\mathrm{a_0}}\right|_{\sigma=90^\circ} \tag{1.21}$$

Here, the positive integer n describes the order of multiples of π. At the Bragg scattering condition, reflection of propagating spin-waves is maximum, causing a minimum in transmission. The minimums in spin-wave transmission spectra are referred to as bandgaps.

Magnonic Resonators

Magnonic crystals are limited in size, as every scattering unit has to be at least half the length of the spin wave wavelength. This is a big challenge for miniaturization. Easier to downscale are other approaches are, e.g., resonators or tunnel barriers, with well defined Eigenfrequencies, that shape the band structure. However, it is often difficult to efficiently trap spin waves inside. One approach is a tunnel barrier. [Krawczyk and Grundler, 2014] A defined frequency pass band then tunnels through the barrier, while other frequencies are reflected. Another one is to trap the spin-wave in between two switchable wires, which induce a reflecting barrier. This method is called a magnetic mirror.[Serga et al., 2009]

2. Methods

2.1 Sample Preparation

PLD Growth of Nanometer-Thin YIG Films

Pulsed laser deposition was used to grow high quality nanometer-thick YIG films with ultralow damping on top of single-crystal (111) – oriented $Gd_3Ga_5O_{12}$ (GGG) substrates. The used PLD system is depicted in Figure 2.1. The main components are a Lambda Physik ComPex 201 excimer laser system, an infrared substrate heating laser ($\lambda = 818\,\text{nm}$ that can heat up to 1000 °C), a vacuum deposition chamber and a load lock chamber. Mechanical and turbo pumps pump down both chambers to a base pressure of about $5 \cdot 10^{-9}$ mbar. The ComPex 201 laser system produces high-power KrF laser pulses with $\lambda = 248\,\text{nm}$, which travel through optical lenses and enter the deposition chamber through the indicated window. In the chamber, YIG target atoms and clusters are ablated by the laser pulses from a stoichiometric target, which then deposit onto the heated GGG substrate. A second chamber is connected to the deposition chamber and serves as a load lock. It can be isolated by a gate valve from the main chamber. The substrate is transferred into the deposition chamber by means of a magnetic transporter. A well defined O_2 atmosphere was established and controlled by using an oxygen inlet and a leak valve. These are indicated by the green inlet and lightblue outlet in Figure 2.1(c).

Following an optimized recipe for high-quality YIG film growth, firstly, the substrates were thoroughly cleaned in acetone and isopropyl alcohol using an ultrasonic bath before loading them into the PLD system. After pumping for 1 h, the sample was transferred into the deposition chamber and slowly ($15\,\frac{°C}{min}$) heated to 870 °C. After reaching 500 °C an O_2-pressure of 0.13 mbar was established. During the deposition, the laser repetition rate was 2 Hz with a fluence of $1.8\,\frac{J}{cm^2}$. The growth speed equated $2\,\frac{nm}{min}$. By varying the growth time, the intended film thickness is set. After deposition, the sample was annealed at 730 °C in 13 mbar O_2-pressure and before cool down to room temperature at a rate of $-3\,\frac{°C}{min}$.

The YIG films grown for this study have a thickness of 100 nm (sample 1) and 43 nm (sample 2 and 3).

VNA–FMR Spectroscopy and Gilbert Damping of As-Grown YIG Films

After growth, every sample was characterized by means of VNA–FMR spectroscopyto evaluate the film properties as damping, anisotropy and saturation magnetization. Measurements were performed by placing the sample face-down onto a coplanar waveguide (CPW). The CPW was connected to a vector network analyzer (VNA) inside a homebuilt microwave probing station with a quadrupole electromagnet. The CPW had a 50 µm wide signal line and two 800 µm ground lines. The gap between the signal and grounds line was 30 µm. A magnetic bias field was applied in the Damon Eshbach geometry, i.e. in-plane and perpendicular to the CPW signal line. By detecting the amplitude and phase of Scattering Parameters, the response of the magnetic film to a microwave excitation signal was recorded. To improve contrast, data is compared to a reference measurement taken at a higher magnetic bias field, e.g. 200 mT. At this point it should be

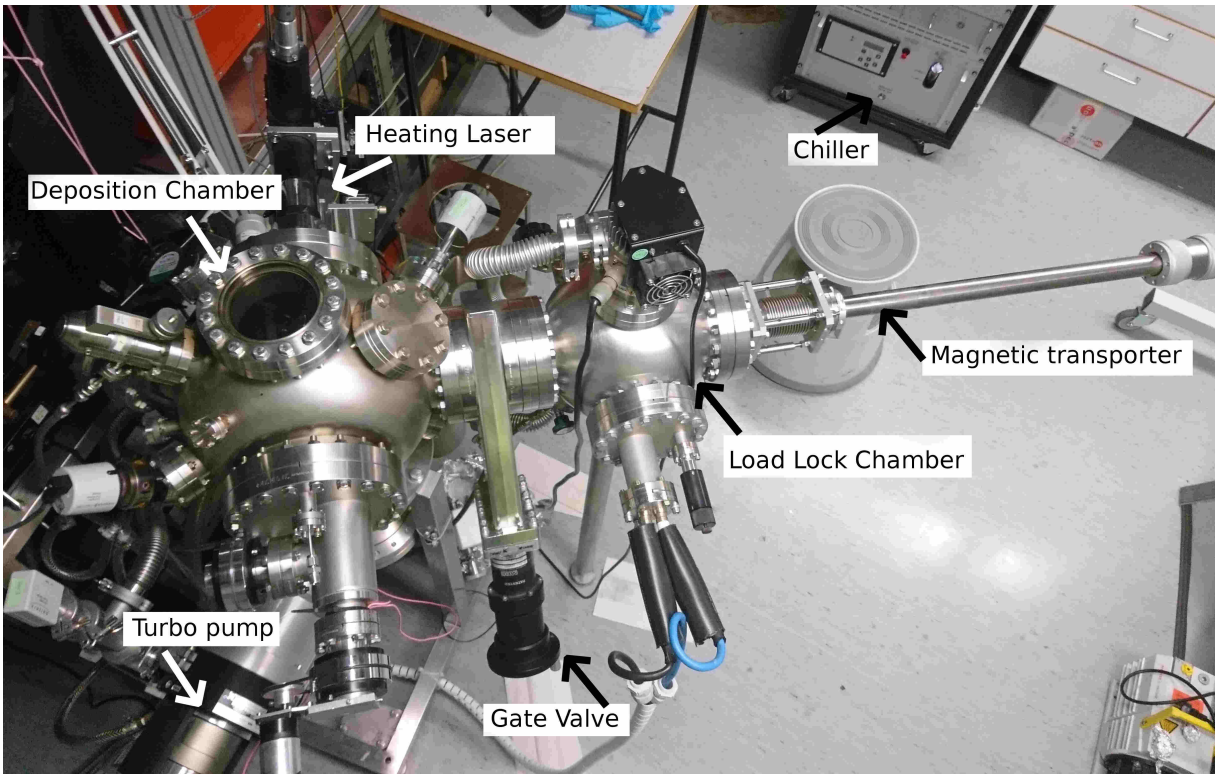

(a)

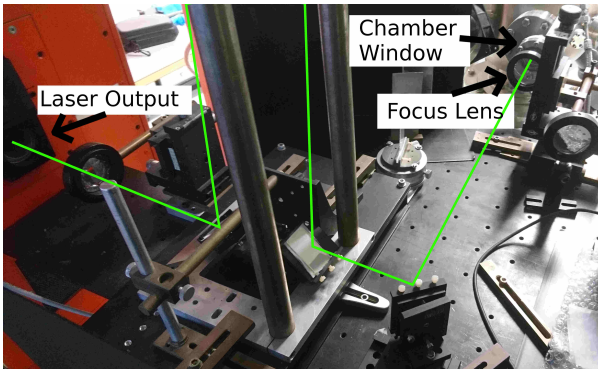

(b)

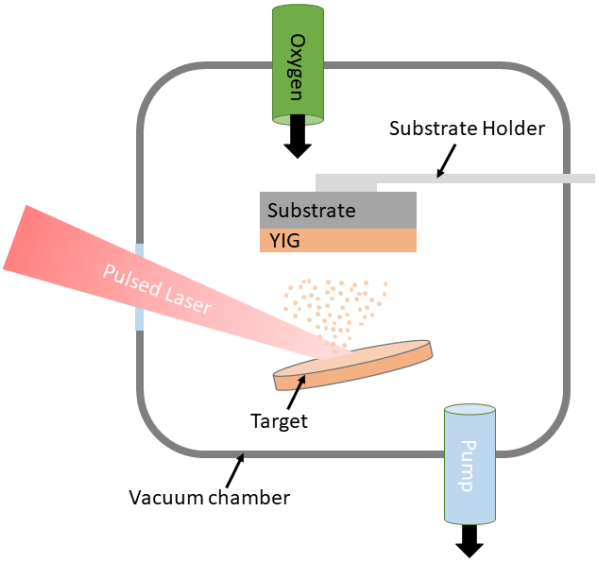

(c)

Figure 2.1: The PLD system. (a) Photo of the PLD system used for YIG film growth. The main components are labeled. (b) Photo of the optical system used to shape the laser pulses before entering the PLD system. (c) Schematic of the PLD growth process.

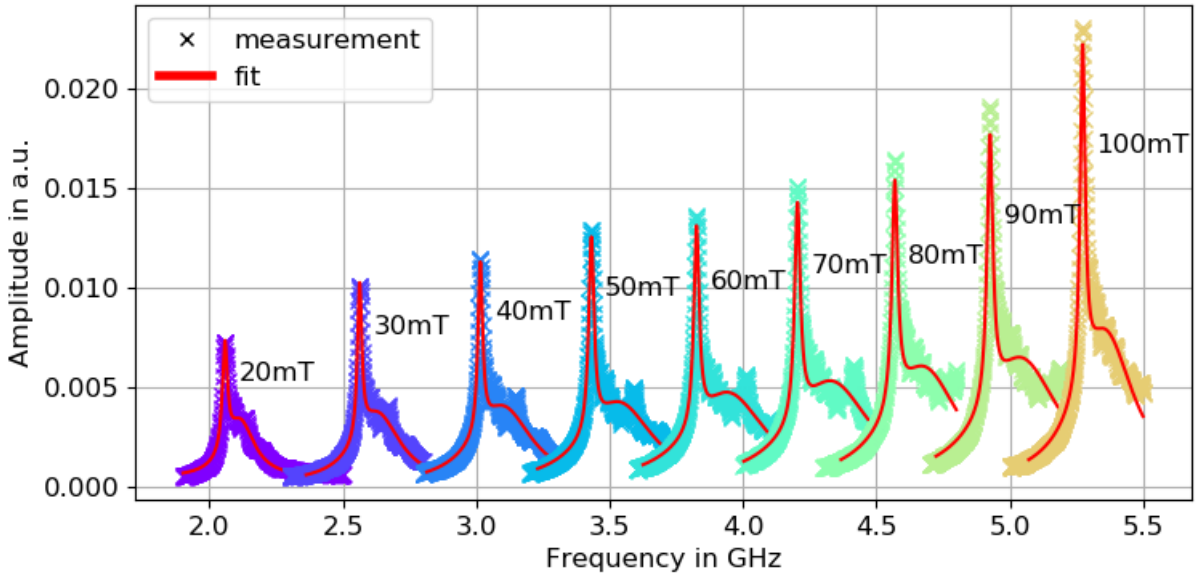

Figure 2.2: Typical results for VNA-FMR measurements from sample 2. Multiple FMR spectra are measured by VNA–FMR spectroscopy. Each colored peak shows the FMR mode with $f_{FMR} = f(k = 0)$ for different magnetic bias fields. Crosses refer to measurements and solid lines to the corresponding fits. Similar results are obtained for sample 1 and sample 3.

mentioned, that a lorentzian signal is expected, however, the data shows asymmetric peaks. This is related to the superposition of resonance and excitation of propagating spin-waves with $k \simeq 0$ induced by the CPW.
Figure 2.2 shows FMR data for sample 2as a function of applied magnetic bias field. Symbols (crosses) correspond to measurement data and the red lines are the fits. The results depicted in Figure 2.3 are deducted from the width and location of the FMR peaks measured on samples 1 (green), 2 (blue) and 3 (red). Here, the blue and red colors correspond to sample 2 and 3, respectively.

By fitting the location of FMR frequency to the Kittel-Formula (equation (1.17) on page 7), the effective saturation magnetization M_{eff} and the anisotropy field $\mu_0 \cdot H_{aniso}$ were evaluated. A $M_{eff} = 192\,\frac{kA}{m}$ was determined for sample 1. Furthermore, sample 2 and sample 3 had higher M_{eff} of $203\,\frac{kA}{m}$ and $208.1\,\frac{kA}{m}$, respectively. $\mu_0 \cdot H_{aniso}$ was relatively small with values ranging from $= -0.55\,mT$ to $-0.06\,mT$. These results were used for further analysis. In addition, the intrinsic Gilbert damping parameter α was evaluated. The FWHM of the FMR peaks were determined and the damping parameters were determined using equation 1.15:

$$FWHM\,(f_{FMR}) = 2\alpha f_{FMR} + \Delta k \nu_{group} \tag{1.15}$$

The Gilbert damping constants for three YIG films were found to range from $3 \cdot 10^{-4}$ to $8 \cdot 10^{-4}$. A summary of experimental parameter analysis is given in Table 2.1. Compared to other literature as in [Gallagher et al., 2016], [Hauser et al., 2016] and [Hauser et al., 2016], the fabricated samples are of comparable quality.

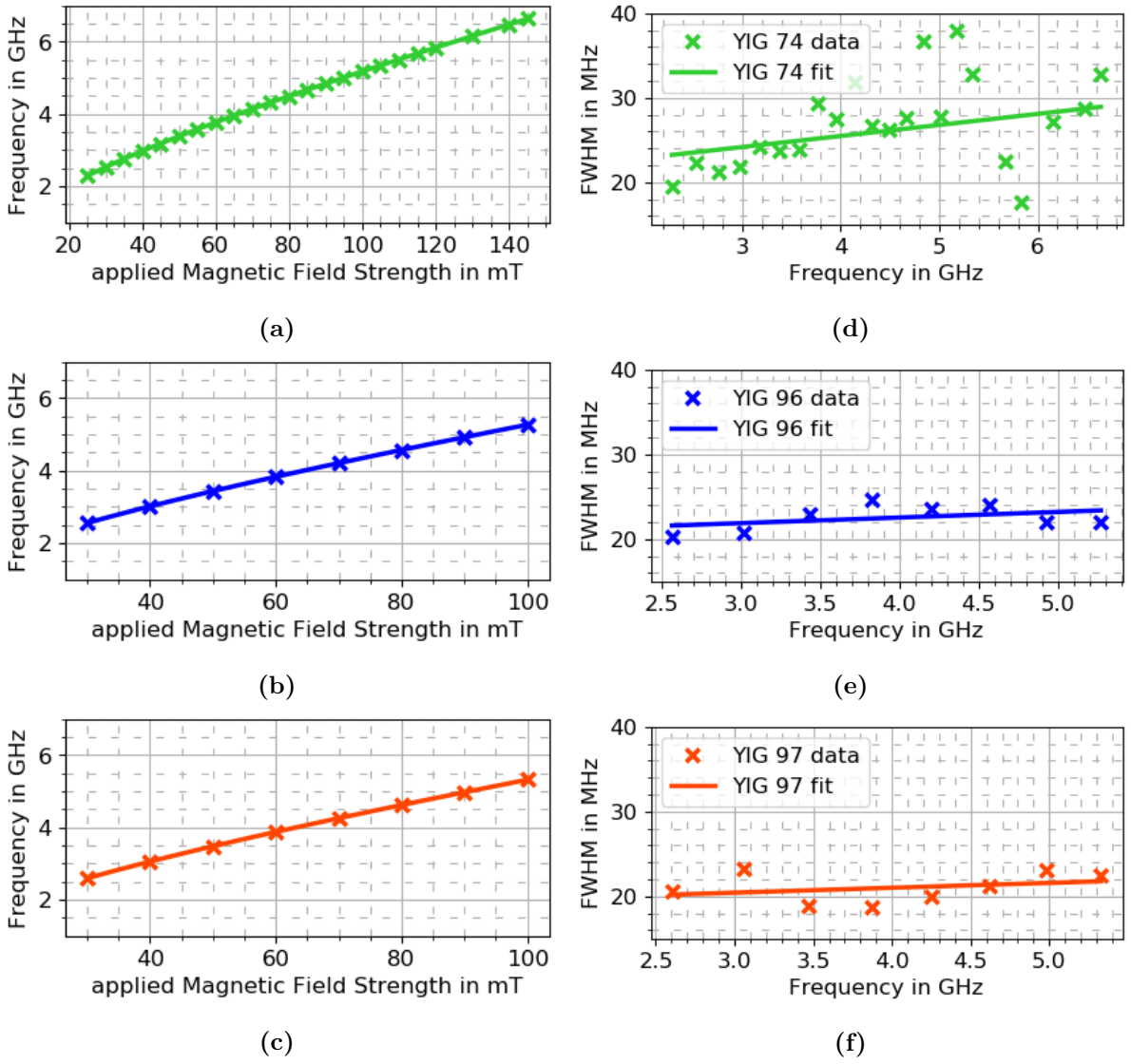

Figure 2.3: Dependence of the FMR frequency and FWHM of the FMR peak on magnetic bias field. The panels show experimental results for samples 1 (green), 2 (blue) and 3 (red). The lines are fits to the experimental data using the Kittel formula (a-c) and equation 1.15 (d-f).

Table 2.1: Summary of experimentally derived values of the saturation magnetization, anisotropy field and damping parameter of the samples in this study. In the first column, the serial number for every sample is given and in the following columns obtained values and properties are listed.

sample	M_{eff} in $\frac{kA}{m}$	$\mu_0 \cdot H_{aniso}$ in mT	thickness d in nm	Gilbert Damping α
sample 1, 74	192	–0.06	100	$8 \cdot 10^{-4}$
sample 2, 96	203	–0.55	43	$3.5 \cdot 10^{-4}$
sample 3, 97	208	–0.36	43	$3 \cdot 10^{-4}$

2.2 Device Fabrication

For this work, two types of structures were fabricated and studied, namely:

Airgroove MCs: These structures consist of several, equally spaced air grooves perpendicular to the spin-wave propagation direction, embedded in the YIG film as depicted in Figure (a). The air grooves have a width w in the range of 0.4 µm to 0.6 µm and a depth d of 6 nm to 18 nm. The periodicity a ranges from 2 µm to 10 µm.

Magnonic resonator array: Four stripes of 50 nm thick CoFeB are grown on top of a continuous YIG film. The width ranges from $w = 0.4$ µm to 2.5 µm and the periodicity from $a =$ 2 µm to 30 µm. A schematic of this structure is displayed in Figure 2.4(b).

Magnonic resonators: As depicted in Figure 2.4(c), these devices are similar to the array structure, but only consist of one single stripe with a width ranging from 0.4 µm to 30 µm.

The fabrication process of the samples is illustrated in Figure 2.5. For structures bigger than 1 µm direct laser writing lithography was used and for smaller patterns we employed electron-beam lithography.
As a first step a polymer resist layer is coated on the sample. To do this, the sample is fixed on a spinning stage (so called spin coater) and the resist fluid is poured over the sample. Spinning at a high rotation speed of 4000 rpm creates an even and thin resist film across the whole sample. For direct laser writing lithography, AZ5214E-resist (1.6 µm thick) is used. For electron-beam lithography, PMMA A4 resist (200 nm thick) capped by an 8 nm aluminum conductive layer is used.
On a heating plate, the monomeric resist is then baked before further processing. Details on the fabrication recipes are given in Table 2.2.

Table 2.2: Parameters used in the fabrication of resist layers for direct laser writing lithography and electron-beam lithography.

Resist	Recipe	Thickness
AZ5214E	30 s at 4000 rpm, baking at 95 °C for 1 min, developing for 45 s	1.6 µm
PMMA A4	1 min at 4000 rpm, baking at 180 °C for 2 min, developing for 15 s	200 nm

In step 2, the resist layer is exposed to a laser or electron beam. To accomplish this, a designed pattern in the form of a *gdsII*- file is used to define the exposure pattern that is written in the resist layer. The polymer bondings in the resist are locally broken by the beam, which makes the monomers soluble in the developer fluid. Using the parameters from previous exposures, the direct laser writing lithography Laserwriter LW405 system is operated using a filter with 1 % transmission. The gain in arbitrary numbers ranged from 20 for big pads and structures bigger than 5 µm width to 25 for structure dimensions of about 2 µm width. The used Laser beam step factor in is 2.

A dose test for the Raith electron-beam lithography system was performed and characterized with AFM. The following optimized parameters were determined. For large structures such as contact pads or orientation markers, a beam current of 90 nA and a dose of 900 $\frac{\mu C}{cm^2}$ was used. The beam diameter assigned to the current was $\sim$ 43 nm. Considering that, a similar sized beam step of 40 nm was chosen. The system calculated the step frequency automatically.

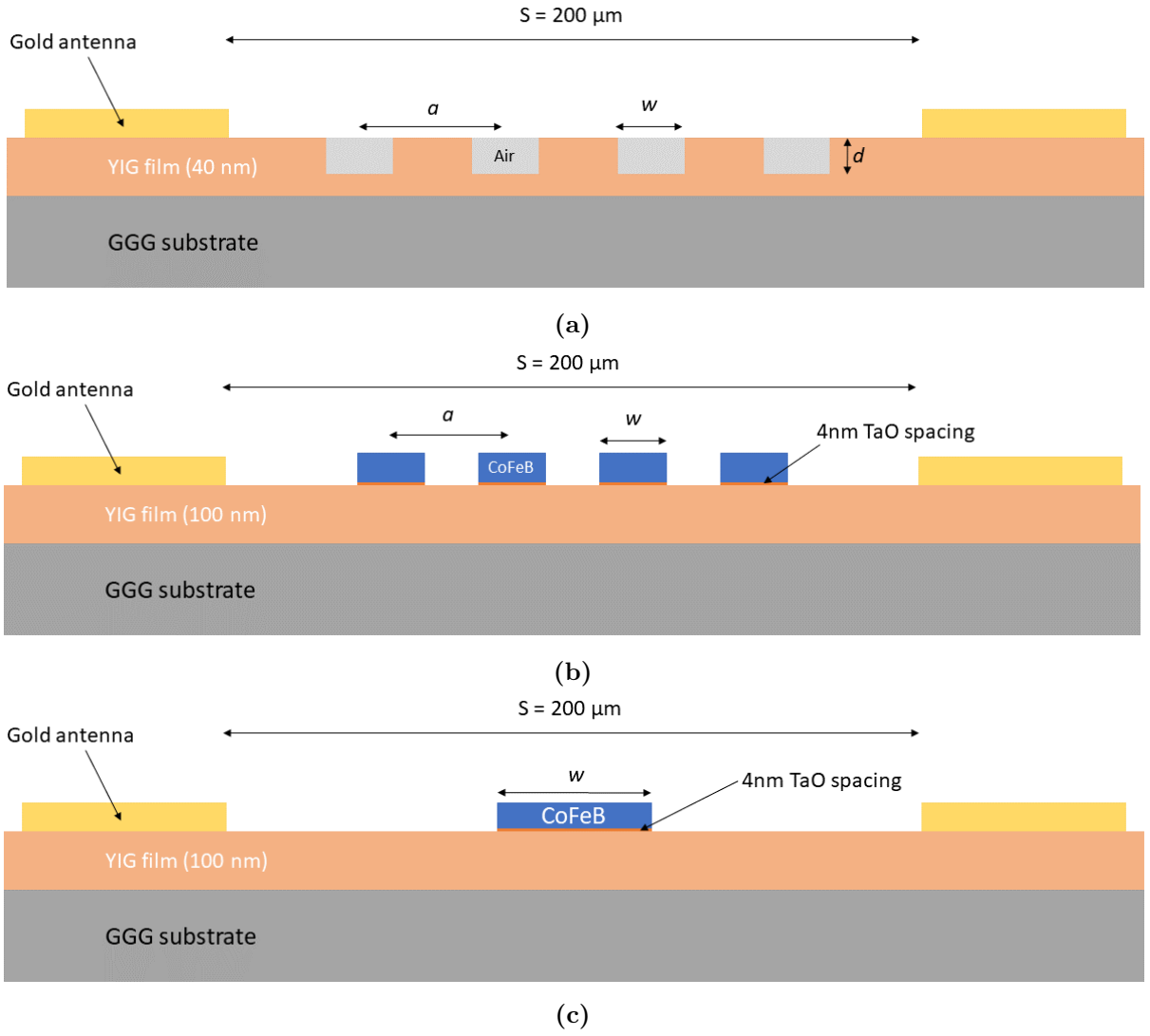

Figure 2.4: Schematics of the structures studied in this thesis (not to scale). The grey base depicts the GGG substrate, which is about 10 x 10 mm^2 and 500 µm thick. It is covered by a patterned (a) or continuous (b,c) YIG film (orange). On top of the YIG films, CoFeB stripes (b,c) and gold microwave antennas (all) are patterned. The left antenna is used for the excitation of propagating spin-waves and the right antenna detects the spin-waves after transmission through the device structure. The antennas are separated by 200 µm.

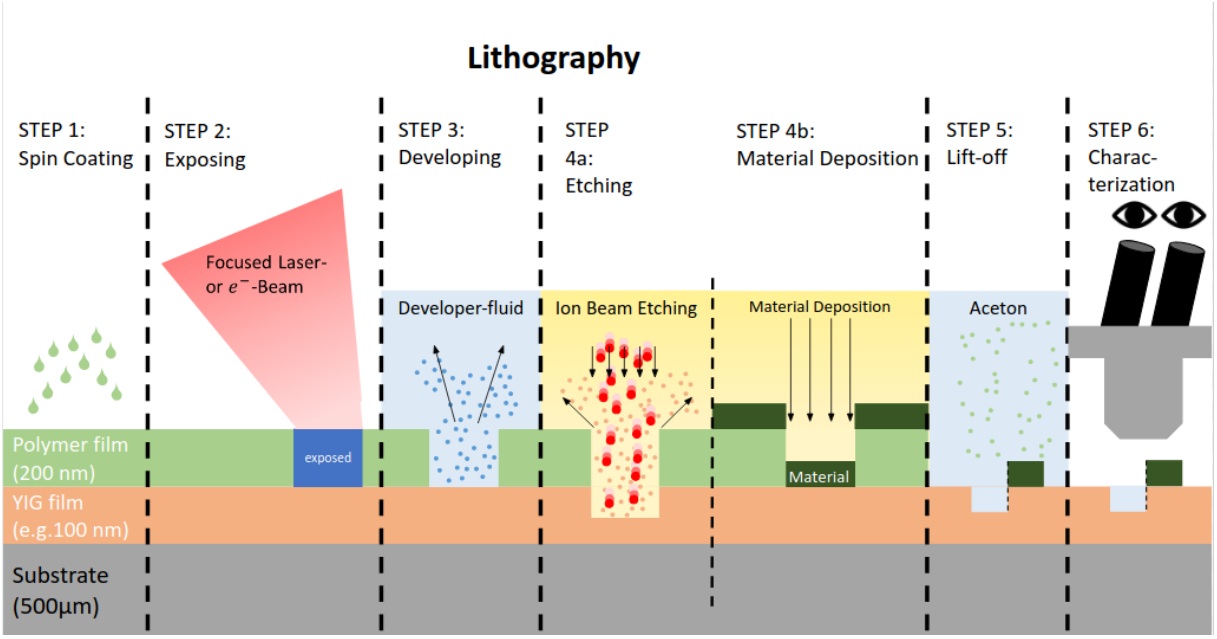

Figure 2.5: Schematic of the device fabrication steps. The sample consists of GGG substrate with an epitaxial YIG thin film on top (grey and orange, respectively). As a first step, a monomeric resistlayer is spin coated on the YIG film and polymerized by baking. In step 2 , a pattern is defined in the resist layer by exposure to a laser beam (direct laser writing lithography) or an electron beam (electron-beam lithography). Next, the resist layer is developed. In step 4, air grooves are patterned using Ar-ion beam milling or CoFeB is deposited using magnetron sputtering. Lastly, resist layer is lift off in acetone. Hence, the designed structure is cropped. After fabrication, the samples are inspected by optical microscopy or atomic force microscopy (AFM).

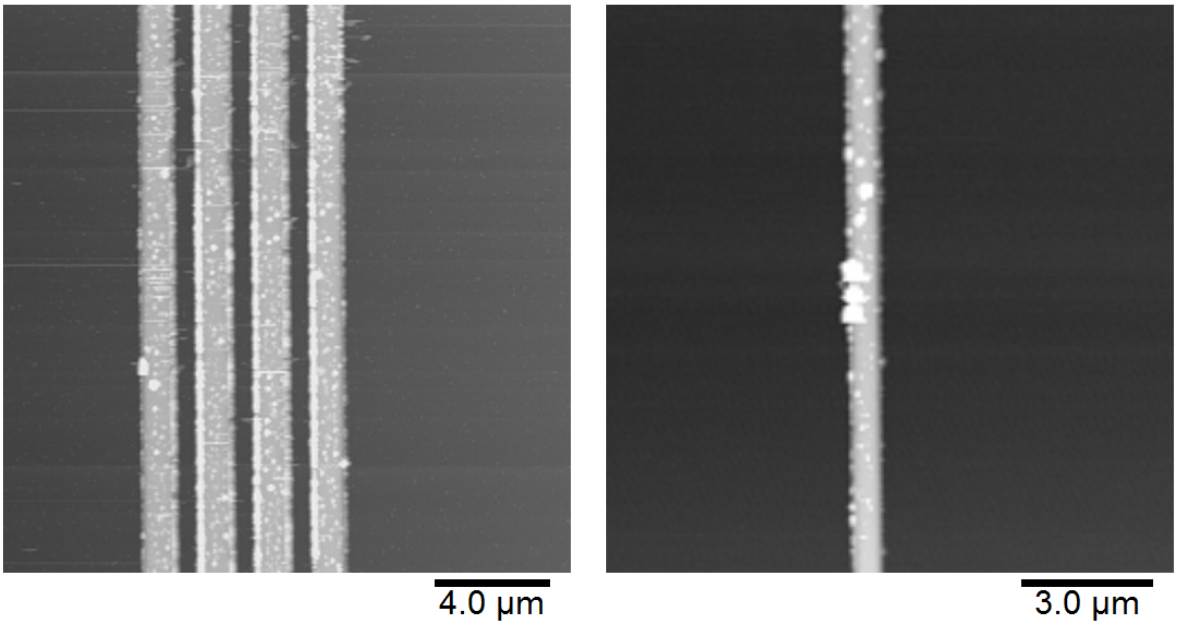

Figure 2.6: AFM images of 50 nm-thick CoFeB stripes on top of a continuous YIG film. On the left, an array consisting of four stripes with 2 µm spacing and 1 µm width . The right image depicts a single CoFeB stripe with a width of 0.7 µm.

For narrow structures, a beam current of 10 nA and a 10 nm beam diameter and step size was used. The dose varied from 1300 $\frac{\mu C}{cm^2}$ for 200 nm stripe width to about 850 $\frac{\mu C}{cm^2}$ for 2000 nm stripe width. For arrays a complex trade off is conducted considering the ratio of width and periodicity.

To obtain the deposition mask, the polymer resist is developed after direct laser writing lithography for exactly 45 s in AZ351B (1:5 Deionized Water). After electron-beam lithography the resist was developed for exactly 15 s in MIBK (1:3 isopropyl alcohol). For electron-beam lithography the conducting Al-layer has to be removed before development by using AZ351B, the developer for direct laser writing lithography. To avoid overdeveloping, the sample is rinsed in DI-water or isopropyl alcohol for AZ351B or MIBK, respectively.

As shown in Figure 2.5, material deposition or etching are conducted next (step 4). The Deposition was done by magnetron sputtering. Here, an automated recipe is used. The air grooves are milled using Ar^+ ions in a Meyer Burger IonSys 500 system. A beam current of 300 nA with an acceleration of 250 V and a milling rate of 6.545 $\frac{nm}{min} = 9.167 \frac{s}{nm}$ were used. The neutralization beam of 250 nA was used to prevent the sample charging.

After material processing, the resist layer is lifted off in acetone and thereby all excess material is removed. Exposure to the electron beam, hot sputter atoms and/or ion bombardment can crystallize the polymer resist near the edges, which can make resist removal difficult. To inspect the quality of the lithography process, microscopy was used. Structures bigger than ~ 500 nm were imaged using optical microscopy, whereas smaller structures were tested using AFM. Figure 2.6 demonstrates that, almost vertical edges with well separated features are fabricated. Bright features at the edges correspond to some residual resist.

2.3 Broadband spin-wave Spectroscopy

spin-wave transmission spectra of magnonic devices were measured with a homebuilt broadband SW spectrometer. The setup is depicted and sketched in Figure 2.7. It consists of an "Agilent Instruments PNA Network Analyzer N5222A" 2-port VNA, a quadrupole magnet and two microwave cables with two Ground-Source-Ground probes (GSG). The VNA provides microwave currents with a frequency ranging from 10 MHz to 26.5 GHz. By means of two power supplies and two Hall sensors, it is possible to apply precise magnetic fields in the range of 0.1 mT to 250 mT along arbitrary angles within the sample plane. The red inset shows a magnified image of the contacting area and the sample mounting. The stereo microscope and the micropositioners are used to connect the microwave antennas via GSG-probes and multiple microwave cables to the VNA and device structures. The green inset magnifies the mounted sample with microwave antennas and probes.

To excite spin-waves, a microwave current is applied to the microwave antenna. In the film, a torque excites the spins to precess. Specifically, this exciting current induces a faraday voltage according to equation 2.1. At the detecting microwave antenna, the voltage is induced vice versa within the wire and is described by equation 2.2. ([Huber, 2013] p.38ff)

$$\mathrm{V_{ind,\ exc}} \propto \int \chi\left(\omega, \mathrm{k}\right) \left|\rho\left(\mathrm{k}\right)\right|^2 \mathrm{dk} \tag{2.1}$$

$$\mathrm{V_{ind,\ det}} \propto \int \chi\left(\omega, \mathrm{k}\right) \left|\rho\left(\mathrm{k}\right)\right|^2 \cdot \mathrm{e}^{-\mathrm{i(ks}-\phi)} \mathrm{dk} \tag{2.2}$$

From tracking the scattering parameters of the ports in the VNA, the transmission amplitude $\mathrm{A_m}$ and phase ϕ_m are obtained. spin-waves recorded in antenna i and excited in antenna j correspond to the Scattering Parameter Sij of the two VNA ports. For positive external bias field, S12 corresponds to +k, for negative bias field, S21 corresponds to –k. To subtract a background signal, a reference measurement is conducted first at high magnetic bias field, i.e., at 130 mT. Using the reference signal ($\mathrm{S_{ref}}$) and the measurement signal ($\mathrm{S_m}$), the corrected amplitude of the scattering parameter is then defined as:

$$\mathrm{S_m} = \mathrm{A_m} \cdot \mathrm{e}^{\mathrm{i} \cdot \phi_\mathrm{m} \cdot \frac{\pi}{180}} \tag{2.3}$$

$$\mathrm{S_{ref}} = \mathrm{A_{ref}} \cdot \mathrm{e}^{\mathrm{i} \cdot \phi_\mathrm{ref} \cdot \frac{\pi}{180}} \tag{2.4}$$

$$\mathrm{A_{corr}} = \frac{\left(\mathrm{S_m} - \mathrm{S_{ref}}\right)}{\mathrm{S_{ref}}} \tag{2.5}$$

When data in plots is normalized, the data is converted to the so called z-score using 2.6. Following [wikipedia.org, 2020], every measurement point $\mathrm{y_i}$ is subtracted by the mean μ of that data set and then divided by the set's standard deviation σ:

$$\mathrm{y_{i,s}} = \frac{\mathrm{y_i} - \mu}{\sigma} + 1 \tag{2.6}$$

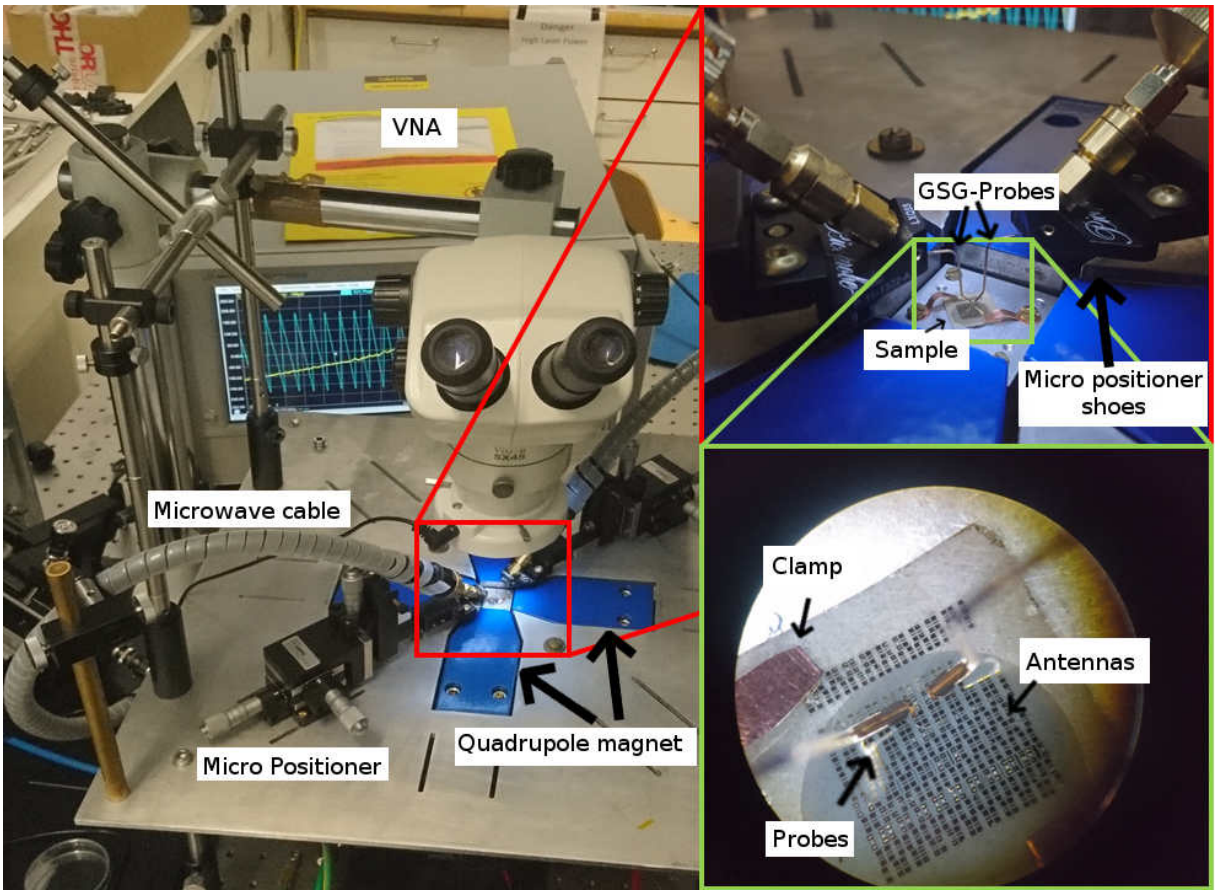

(a)

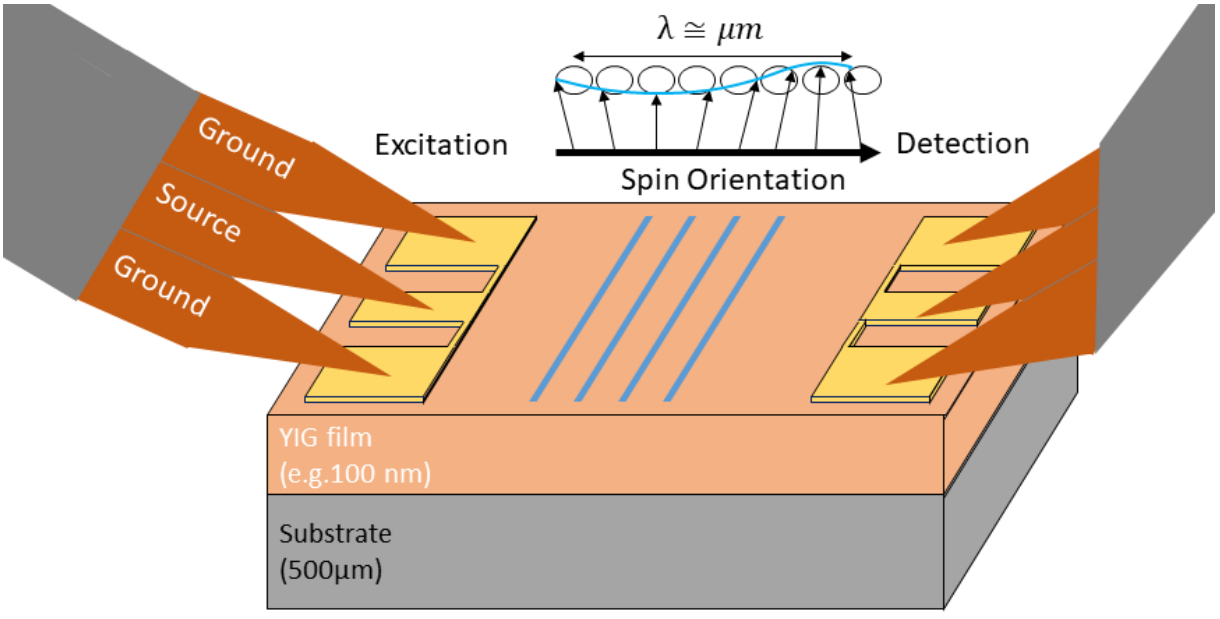

(b)

Figure 2.7: Broadband spin-wave spectroscopy measurement setup. In the setup, the microwave antennas on the samples are contacted by GSG probes and connected to a VNA via microwave cables. The quadrupole electromagnet is embedded in the sample stage allowing the application of a magnetic bias field along arbitrary in-plane directions.

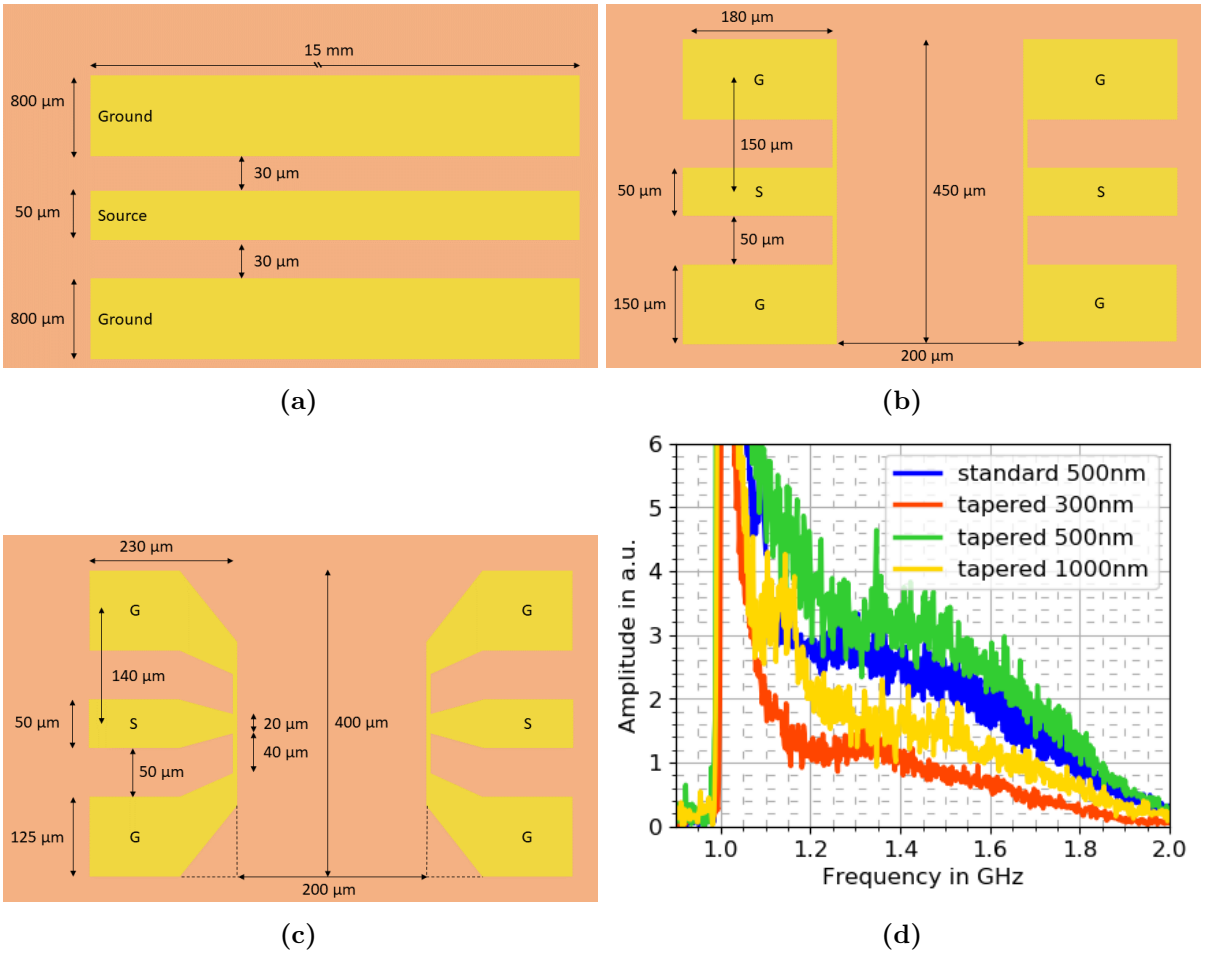

Figure 2.8: Schematic of microwave antennas and contact pads used in this study. The antennas shown in yellow are made from gold. (a) The CPW used for VNA–FMR spectroscopy. Note the varying length units! This CPW consists of a source line in between two ground lines. The structure is symmetric around the source line axis. (b) Former design and (c) for this study used Microwave antenna designs. The microwave antenna lengths are 50 µm and 40 µm, respectively. The width is 0.5 µm for both. (d) spin-wave transmission spectra of different antenna widths and designs. The blue plot refers to the spin-wave transmission spectrum of a formerly used design fabricated with 50 µm long, 0.5 µm wide antennas, and straight contact pads. Yellow, green and red refer to 1000, 500, and 300 µm wide and tapered designs with 40 µm long microwave antennas.

Antenna and Contact Pad Design

Figure 2.8 shows different designs of microwave antennas for spin-wave excitation. The CPW displayed in Figure 2.8(a) was used in VNA–FMR spectroscopy. The second design shown in Figure 2.8(b) has been used formerly for broadband SW spectroscopy. From this design, the optimized antenna design in Figure 2.8(c) is derived. The excitation range, i.e. the highest excited wave number, of microwave antenna is proportional to its inverse width. Thus, a narrower antenna can excite higher wavenumbers. However, the signal prominence decreases. The signal and ground lines have the form of a CPW The impedance of this CPW is matched to 50 Ω and shorted at one end. Varying antenna widths from 6 µm to 0.3 µm and lengths from 70 µm to 35 µm were investigated. The dependecy of transmission spectra to wire width and length is plotted in Figure 2.8(d) A design with 500 nm wide and 40 µm long antenna provides a trade off of high signal prominence and far excitation range. To keep the same GSG probes and hence spacing of signal and ground lines, the ends had to be tilted/tapered.

3. Results and Discussion

This chapter summarizes the results obtained from three types of devices allowing of active manipulation of spin-wave transmission in the Damon Eshbach geometry.

In the first section, results of YIG-based MCs with air grooves are presented and discussed. The results are related to other works such as [Qin et al., 2018], [Chumak et al., 2009], [Filimonov et al., 2012].

In the second section, spin-wave transmission spectra measured on devices with an array of four 50 nm thick CoFeB stripes patterned on top of a continuous 100 nm thick YIG film are presented. It is shown that the YIG/CoFeB bilayer acts as a resonator that opens gaps in spin-wave transmission spectra at discrete frequencies if the width of the CoFeB stripes is smaller than 10 µm without affecting the spin-wave signal at allowed frequencies. Moreover, the same structures provides nearly full transmission non-reciprocity if the CoFeB stripe is wider than 25 µm. Both effects are explained by different down-conversions of the spin-wave wavelength in the bilayer for positive and negative wave vectors. As shown in this section, the new bandgap opening mechanism also works utilizing a single stripe.

In the third section, a model is derived from an extension of the analytical model in [Grünberg, 1981] to accurately describe the effects by taking into account exchange coupling within each of the two magnetic layers. Using a plane-wave approximation, a resonance condition is derived which, in combination with the analytical model, provides accurate predictions of the frequency gaps in spin-wave transmission spectra.

3.1 Air Groove–based Magnonic Crystals

Various YIG-based MCs with air groove were fabricated from 43 nm thick YIG film. Every device is determined by the lattice constant "a", the groove width "w" and a number of air grooves "N". Typically, four air grooves were patterned in between two microwave antennas.

Figure 3.1 shows contour plots of spin-wave transmission spectra (amplitude of S12 scattering parameter) for an applied magnetic bias field of –10 mT to 10 mT and 40 mT to 60 mT. Additionally, line profiles are plotted for 4 mT and 50 mT. The device consists of four 0.5 µm wide grooves, 12 nm groove depth, and a lattice constant of 2 µm. This results in a combined size of only 7.5 µm. On the right side of the Figure, the dispersion for magnetostatic surface spin-waves is shown by the blue line. The purple and red lines indicate the first and second order Bragg scattering condition.

$$\mathrm{k} = \left.\frac{\mathrm{n}\cdot\pi}{\mathrm{a}}\right|_{\mathrm{n}\in\mathbb{N}} = \mathrm{n}\cdot 1.571\left.\frac{1}{\mu\mathrm{m}}\right|_{\mathrm{a}=2\,\mu\mathrm{m}} \tag{3.1}$$

Both contour plots depict clear and prominent spectra. The lowest excitation frequency corresponds to the FMR signal Above the FMR frequency, propagating spin waves are transmitted well in three allowed bands, whereas their transmission is reduced in the bandgaps corresponding to n = 1 and n = 2. The bandgaps agree very well with frequencies as predicted by the dispersion relation and Bragg scattering conditions (see plots on the right and dashed lines).

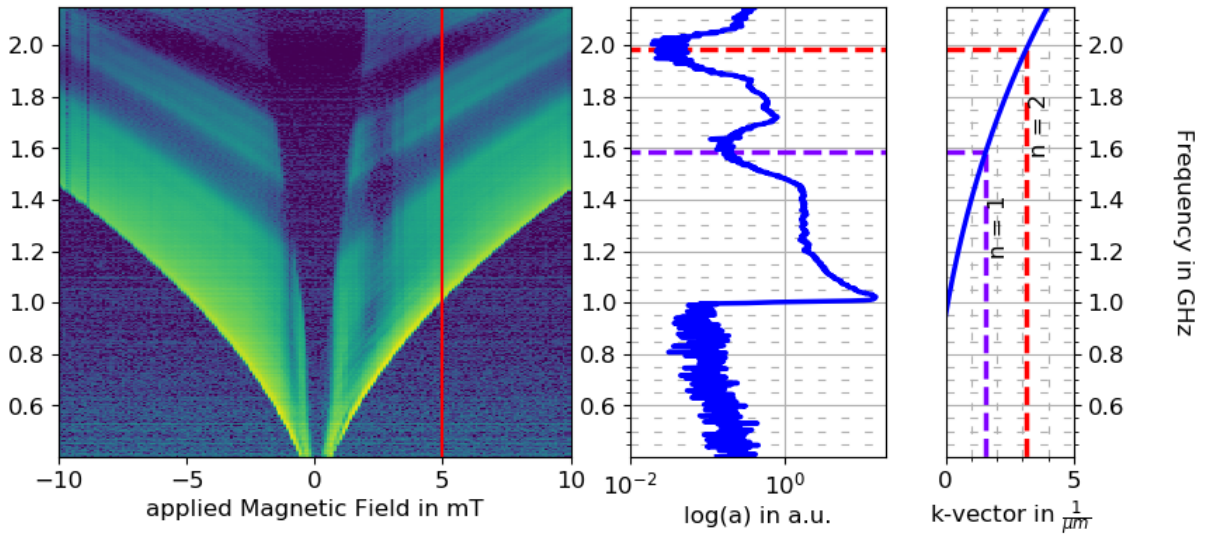

(a)

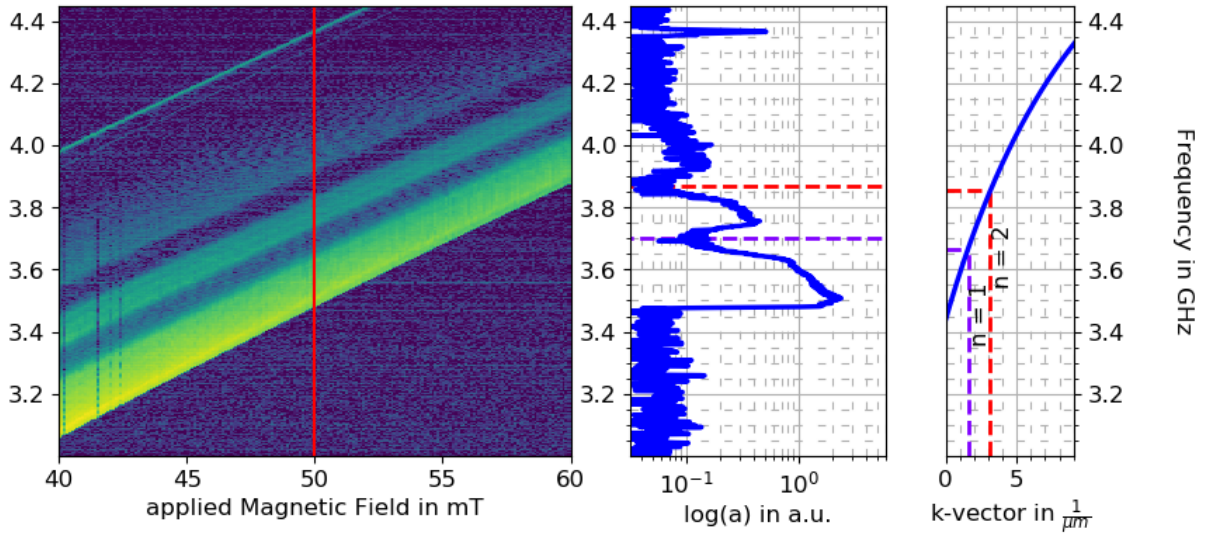

(b)

Figure 3.1: Contour plots of spin-wave transmission spectra for two different ranges of the magnetic bias field. The sample consist of a 43 nm thick YIG film with four air grooves. The period of the lattice is 2 µm and the grooves are 0.5 µm wide and 12 nm deep. The right panels show spin-wave transmission spectra at a bias field of 5 mT (a) and 50 mT (b). The bandgaps open up because of Bragg scattering (n = 1 and n = 2) as illustrated by the dispersion curves and dashed lines.

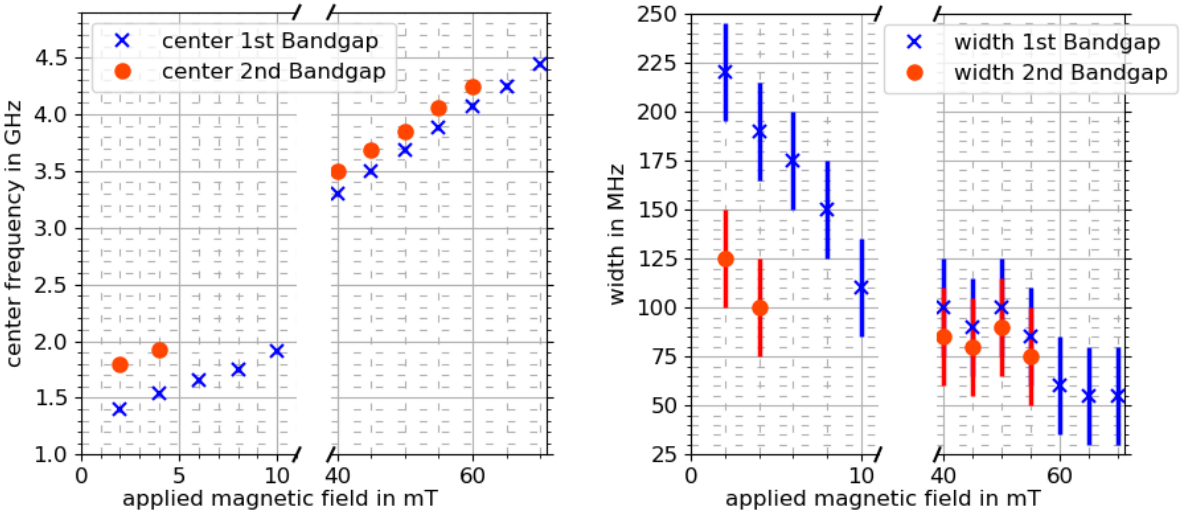

(a) (b)

Figure 3.2: Position of the bandgap frequency (a) and the bangap width (b) as a function of magnetic bias field for the same MC as in Figure3.1. Because the n = 2 bandgap is close to the end of excitation range less data than for the n = 1 bandgap could be extracted. The plot on the right side contains the width of first and second bandgap. The width is measured in MHz. The error for bandgap width is depicted by the size of error bars and amounts ±25 MHz. The error for the bandgap center is smaller than the markersize.

Within the next pages, the transmission spectra of YIG-based MCs with different lattice and groove parameters are presented. Firstly, spin-wave transmission spectra of a typical MC is compared to measurements on a continuous, non-patterned YIG film. Next, parameters like the lattice period (fig. 3.4), groove width (fig. 3.5) and groove depth (fig. 3.6) are varied systematically to gauge their effect on spin-wave transmission spectra and the formation of bangaps.

3.1.1 Comparison of air groove MC to bare YIG

Figure 3.3 depicts a comparison of a spin-wave transmission spectra recorded on a YIG-based MC with an unpatterned YIG film. The structure of the MC comprises four grooves with a lattice period of 2 µm, a groove width of 0.5 µm, and a groove depth of 12 nm (in a 43 nm thick YIG film). The presented data is measured in a 45 mT magnetic bias field.

Multiple features are shown. Firstly, the FMR frequency is about 3.3 GHz. The signal in the first pass band (3.3 GHz to 3.45 GHz) is prominent and the transmission loss in the MC relative to that of the continuous YIG film is only 12.5 %. The signal loss in the second pass band (3.55 GHz to 3.65 GHz) increases to about 32 %. Signal suppression in bandgaps is strong. For example in the first bandgap, the signal is rejected by 85 % comparedto the unpatterned reference. In the work by [Chumak et al., 2009], a 5.7 mm large MC was use. The MC with N = 20 air grooves and a depth of 2 µm on a 5.5 µm YIG film produced a loss of about –12.5 dB or 75 % in the first pass band. In that study, the depth of the first bandgap was –26 dB or 95 %. Results by [Filimonov et al., 2012] are similar to those of [Chumak et al., 2009]. For this study, a 14.7 µm thick YIG film was patterned with 20 air grooves with a lattice period of 150 µm, a groove width of 80 µm, and a groove depth of 1.8 µm. The first pass band had a loss of approximately –12 dB, while the first bandgap had a suppression of –40 dB = 99 %. As displayed in Figure 3.2,

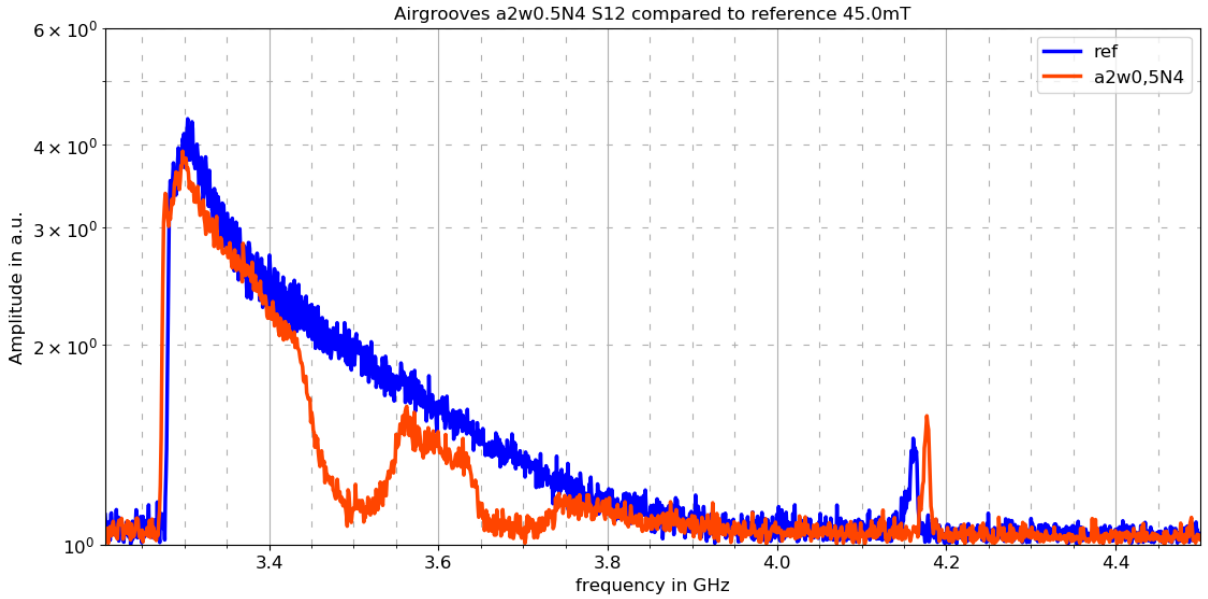

Figure 3.3: spin-wave transmission spectra of a continuous YIG film (blue) and a YIG-based MC with four air grooves. The period of the grooves is 2 µm and their width and depth are 0.5 µm and 12 nm (in a 43 nm thick YIG film). The magnetic bias field is 45 mT.

increasing the applied magnetic field shifts the FMR and the bandgap frequencies up. Thus, it is possible to open bandgaps in a range from 1.5 GHz to 4.5 GHz for magnetic field in the range of 5 mT to 70 mT. In the same magnetic field range the width of the first bandgap ranges from ∼ 220 MHz to 50 MHz. In [Chumak et al., 2009], the width of the bandgaps can be estimated as ∼ 10 MHz. Similar value is found in [Filimonov et al., 2012]. Above 3.9 GHz, the transmission signal of spin-waves vanishes for both, bare YIG in blue and patterned YIG in red. The excitation range of 0.65 GHz stays the same even after patterning. Transformed into reciprocal space, this results in a k-range of k = 0 $\frac{1}{\mu m}$ to 1.44 $\frac{1}{\mu m}$.

3.1.2 Variation of various Device Parameters

Lattice Period *a*

As explained in section 1.3, MCs can modify the spin-wave dispersion by scattering at periodic potentials. The scattering condition is given by Bragg's law. Figure 3.4 (a) shows spin-wave transmission spectra for various lattice periods *a*. The blue graph depicts the a reference measurement performed on an unpatterned YIG film. The red curve corresponds to result for a MC with N = 4, a = 2 µm, w = 0.5 µm, and d = 12 nm, so the same as in Figure 3.3. In addition, green graph show results for a = 5 µm and the yellow curve denotes data for a = 10 µm. The depth of bandgaps varies with the Bragg scattering order n. The higher the wave number k, the stronger is suppression of the signal within bandgaps. This becomes very distinct for a = 10 µm. The first bandgap located at 3.28 GHz is shallow. Within the first five bandgaps, the signal suppression increases until signal is almost suppressed down to background level. The sixth bandgap at 3.52 GHz and higher frequency are able to suppress measured signal strength completely. The feature with a lattice constant of 5 µm, displayed in green, has bandgaps with overall deeper and wider characteristics than *a* = 10 µm. Since the lattice constant is smaller, the distance between bandgaps is increased to approximately 90 MHz to 100 MHz. Similar performance is observed for

Table 3.1: Summary of parameters for the first band gaps in Figure 3.5. The first column gives structure specifications as in lattice constant, width and number of air grooves in the evaluated MC. The neighboring column describes the frequency of the first bandgap. In the last column the FWHM of the bandgap is given.
Spin-wave transmission spectra for MCs with different air groove depth. Red and green curves correspond to a groove depth of 12 and 18 nm, respectively. Measurement data for an unpatterned YIG film is plotted in blue.

structure	x_0 in GHz	FWHM in MHz
$a2w0.4N4$	3.50 ± 0.02	50 ± 10
$a2w0.5N4$	3.51 ± 0.02	80 ± 10
$a2w0.6N4$	3.53 ± 0.02	90 ± 10

other air groove MCs.
As can be seen, the spacing between bandgaps is inversely proportional to the lattice constant. This leads to more and narrower bandgaps when the lattice period is enhanced. In Figure 3.4 (b), the measured bandgap frequencies are compared with calculated values. The bandgap frequencies according to Bragg's law and the dispersion relation of YIG are plotted as green solid lines for multiple scattering orders. The experimental data for a lattice constant of 2, 5 and 10 µm are also displayed. Red solid dots refer to experimental results for a lattice constant of 2 µm. Only gaps up to second order are observed in this case. Up to fourth order bandgaps are visible for a lattice constant of 5 µm shown by green triangles. For a lattice constant of 10 µm (yellow squares) up to 10th order bandgaps are measured. Here, even up to 10th order is measurable. The experimental data and calculations agree well.

Width *w*

Another parameter that can be used to tune spin-wave transmission spectra is the groove width *w*. To analyze this dependency, three different air groove MCs were fabricated. Figure 3.5 shows normalized amplitude of spin-wave transmission for a groove width of 400, 500 and 600 nm are plotted in red, green and yellow, respectively. For comparison, the transmission spectrum of an unpatterned YIG film is plotted in blue.
The results suggest that narrow grooves do not provide deep bandgaps, however broad bandgaps as in 600 nm suffer from larger losses. In table 3.1, the bandgap center and FWHM are presented.

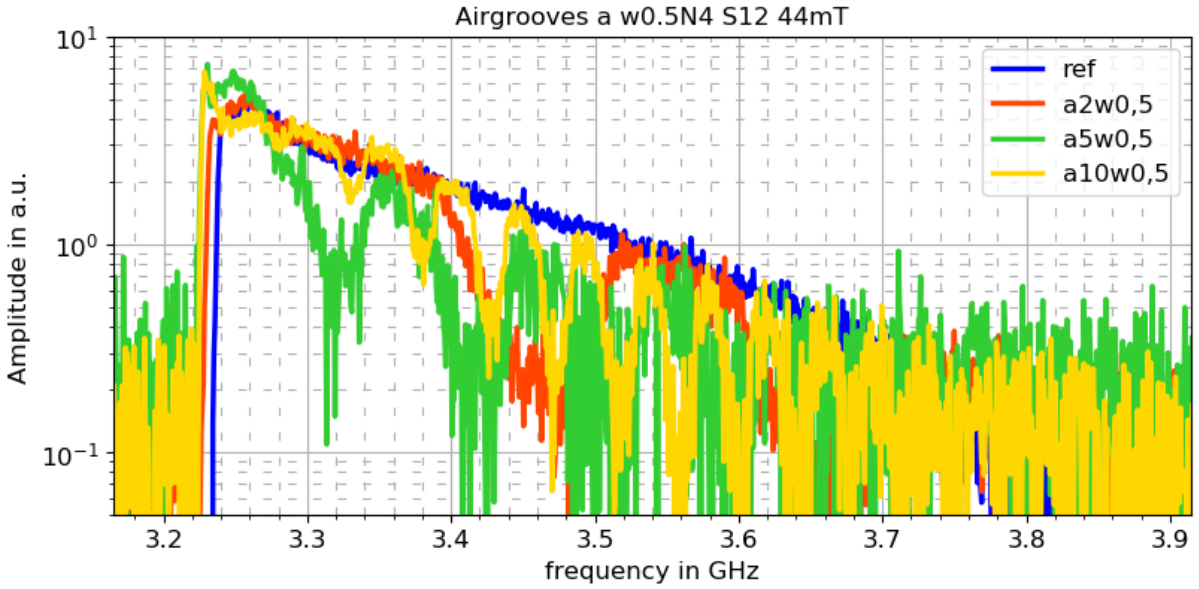

(a)

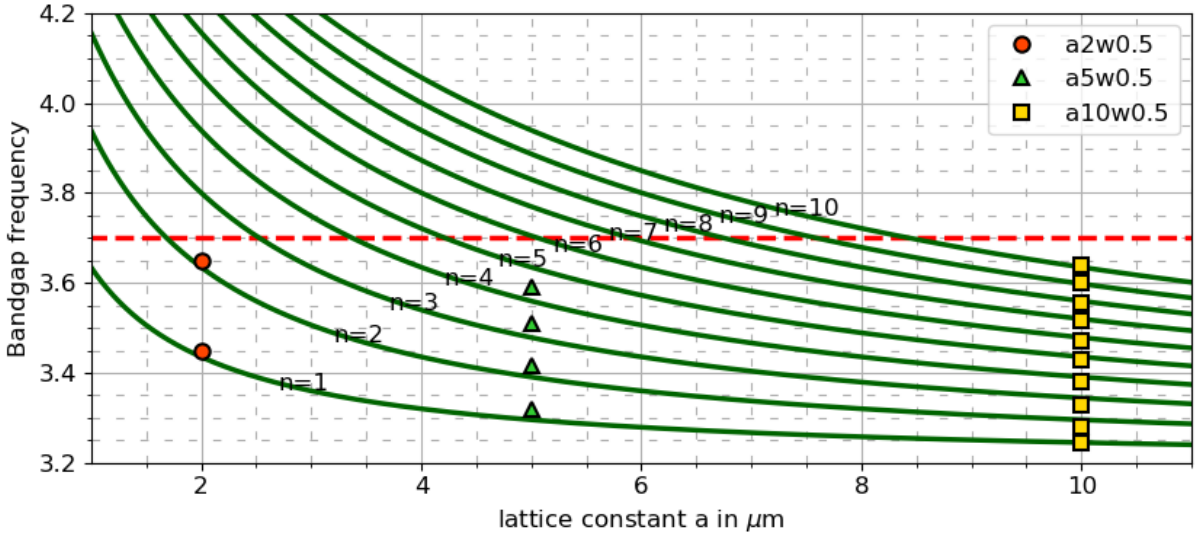

(b)

Figure 3.4: (a), Comparison of spin-wave transmission spectra for three MCs with different lattice constants and a continuous YIG film. Red, green and yellow curves correspond to a lattice constant of 2, 5 and 10 µm, respectively. Measurement data for an unpatterned YIG film is plotted in blue. (b), Calculated bandgap frequency as a function of lattice constant as calculated for different orders of the Bragg condition using the YIG dispersion relation. Experimental data for MCs with a lattice constant of 2, 5 and 10 µm are plotted as symbols. The dashed red line points out the excitation range of the microwave antenna.

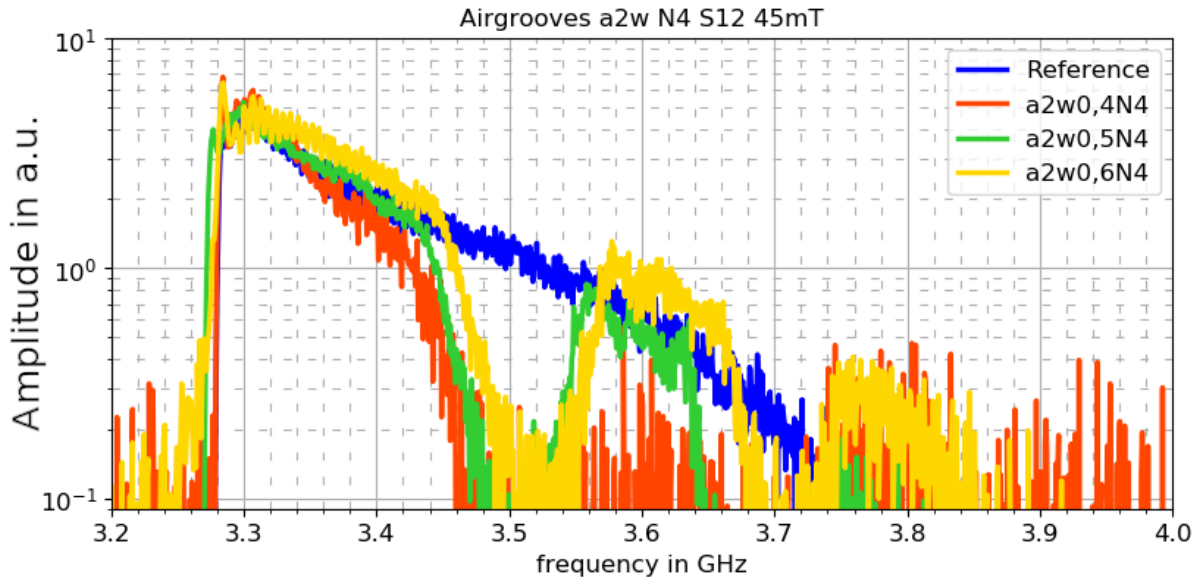

Figure 3.5: Spin-wave transmission spectra for MCs with different air groove width. Red, green and yellow curves correspond to a groove width of 400, 500 and 600 nm, respectively. Measurement data for an unpatterned YIG film is plotted in blue.

Depth *d*

To investigate the effect of the groove depth, MCs with 18 nm deep grooves where patterned in addition to the 12 nm deep ones (both in 43 nm thick YIG films). The corresponding spin-wave transmission spectra are shown in Figure 3.6. For the shallower air grooves, the transmission of spin-waves is efficient. For the deeper air grooves, in contrast, a drastic drop of the transmitted signal is observed. This effect is most likely explained by a deterioration of the YIG film quality underneath the grooves, caused by ion-beam milling during fabrication.
If the air grooves are milled too deep, the left over YIG is damaged, so that the magnetic parameters are heavily influenced. It is not investigated, how much the transmission loss is enhanced or affected by the antenna connection or fabrication.

Other publications as for example [Chumak et al., 2009] a proportionality of depth and loss is discussed as well. There, the signal loss in the first pass band amounts 83 % to 92 % less transmission for 0 µm to 2.5 µm milling depth, i.e., 0 % to 45 % depth.

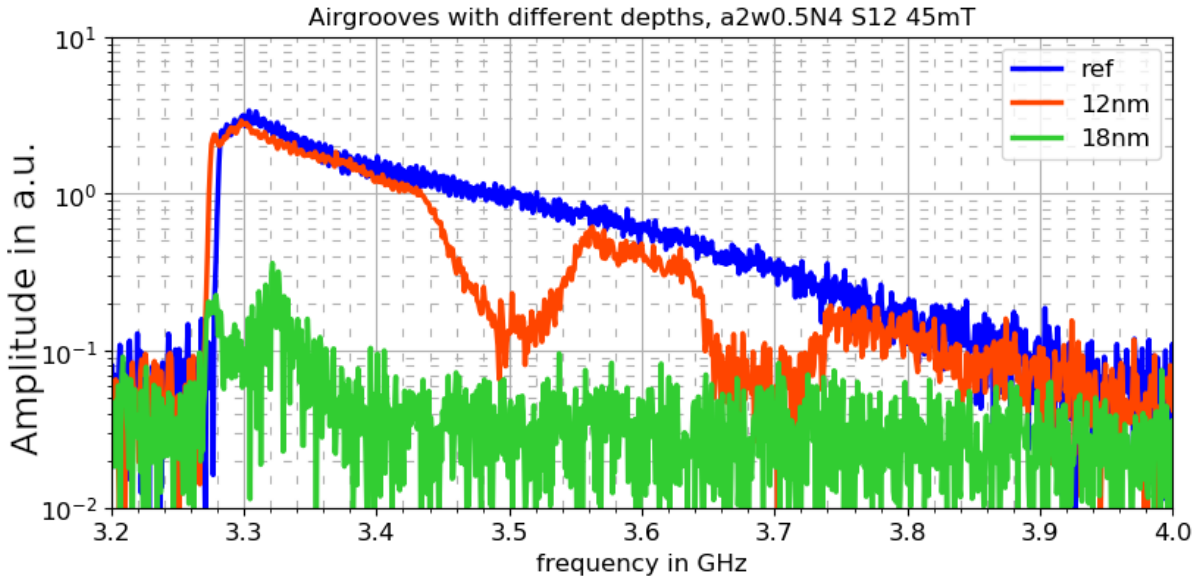

Figure 3.6: spin-wave transmission spectra for MCs with different air groove depth. Red and green curves correspond to a groove depth of 12 and 18 nm, respectively. Measurement data for an unpatterned YIG film is plotted in blue.

3.2 YIG-Based Magnonic Resonators

In the first part of this thesis, active control of spin-waves by YIG-based MCs was demonstrated. However, as ion milling of grooves damages the low damping properties of YIG near the milling edges and in the remaining YIG underneath the air grooves, further down scaling to nanoscale is challenging. As an alternative, a new method for spin-wave manipulation in YIG that does not require patterning of the YIG film itself is presented here.

Figure 3.7 shows contour plots of spin-wave transmission spectra from resonators made of 50 nm thick CoFeB stripes on top of continuous 100 nm thick YIG film (see Figure 2.4 (b,c)). In Figure 3.7(a), the stripe spacing is 2 µm and the stripe width is 0.4 µm. In Figure 3.7(b), only a single stripe with 0.4 µm width was patterned. In addition, line profiles for a magnetic bias field of 4 mT are depicted in the center panels. The right panels show the calculated dispersion curves for magnetostatic surface spin-waves based on equation 1.16 and experimentally derived input parameters for YIG.

It is found, that the bandgaps are not originated from Bragg scattering. The bandgap frequencies for Bragg scattering (indicated in purple) are shifted up to the end or out of the antenna excitation range.
Instead, the new device type provide new features such as nonreciprocity and these magnonic resonators are fully functional also for single stripes. By comparing the scattering parameters S12 and S21, the dispersion branches +k and –k are compared. In Figure 3.8, the non-reciprocity is depicted. The spin-wave transmission spectra corresponding to S12/+k and S21/–k are displayed in blue and red, respectively. The bilayer bandgap is opened at 1.3 GHz. When comparing measurements from S12/+k to S21/–k the rejection shrinks from about 55 % to approximately 38 %. Even a single resonators is able to open bandgaps in spin-wave transmission which enables downscaling to about 400 nm.

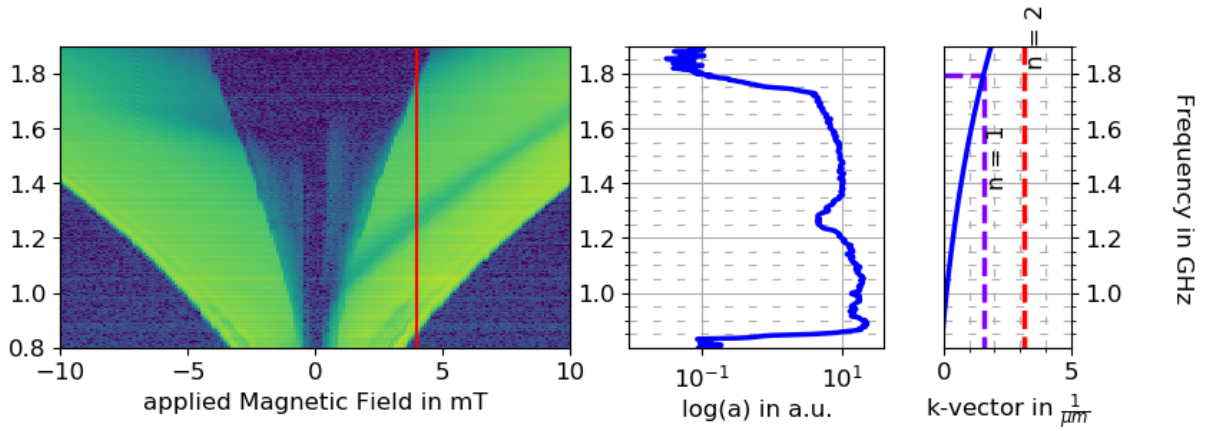

(a)

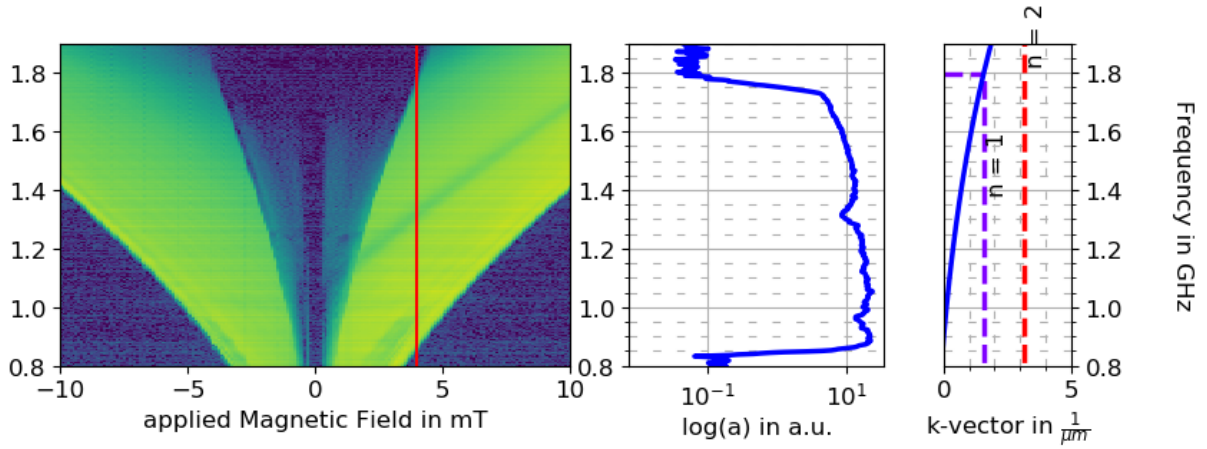

(b)

Figure 3.7: Contour plots for spin-wave transmission spectra for a magnonic resonator with (a) four CoFeB stripes and (b) single stripe. The device consists of 100 nm thick and continuous YIG with 50 nm thick CoFeB stripes patterned on top. (a) Four stripes were fabricated with a periodicity of 2 µm and a stripe width of 0.4 µm. (b) One single stripe is patterned with a width of also 0.4 µm. In the middle panels, the line profiles for 4 mT are shown (indicated by red line). The right panels show the dispersion relation of magnetostatic surface spin-wave. The dashed lines denote bandgap frequencies predicted by Bragg scattering.

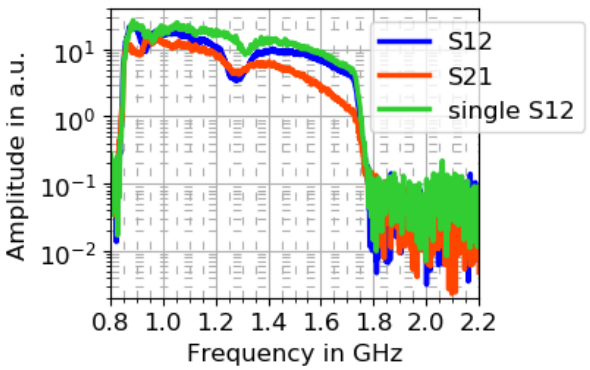

Figure 3.8: Amplitude comparison of scattering parameters S21 and S12 from magnonic resonator array (blue and red) and scattering parameter S12 from single magnonic resonator. The magnonic resonator is made from 50 nm thick CoFeB-stripes on 100 nm YIG film. S12 corresponds to +k and S21 to –k.

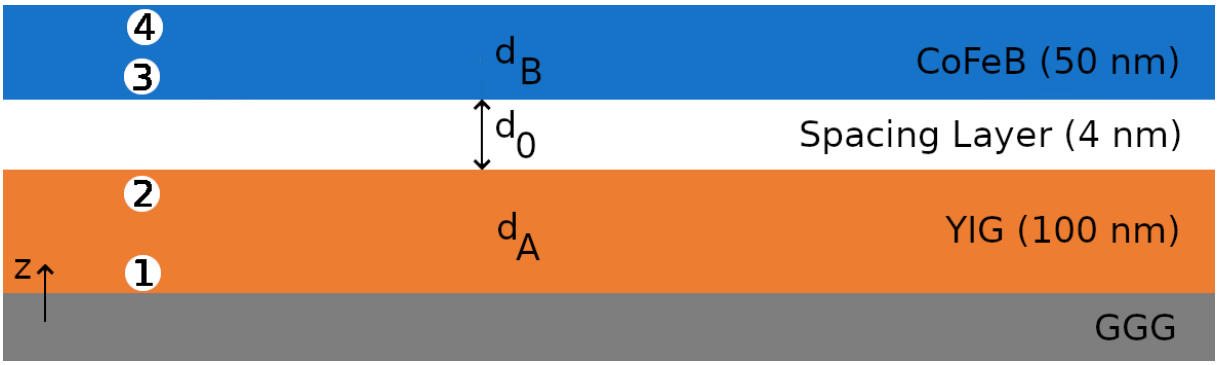

Figure 3.9: Schematic of the bilayer. The grey base corresponds to the GGG substrate. Slab A in orange refers to YIG with thickness d_A of 100 nm and slab B in blue refers to CoFeB with a thickness d_B of 50 nm. The spacing layer has a thickness of $d_0 = 4$ nm. The number 1–4 refer to the localization of the four possible propagating spin-wave modes.

3.2.1 Dispersion of Spin-Waves in a YIG CoFeB Bilayer

Phenomenologically, the mechanism in the magnonic resonator devices is explained by resonant scattering of spin-waves in the bilayer in combination with highly asymmetric downshift of spin-wave wavelength in the YIG-film within the bilayer region. At every device border, the spin-wave is partially transmitted and partially reflected. When transmitted from bare, uncovered YIG (orange) into the bilayer region (blue), the energy and also frequency of the spin-wave is conserved. However, the dispersion is altered and, thus, the wavelength shrinks. Depending on propagation direction, the wavelength shrinks by either only a few percent (–k) or approximately one order of magnitude (+k).
This large wavelength change leads to a phase difference of initial and double reflected waves for narrow stripes. If the frequency fulfills the resonance condition, destructive interference blocks transmission and opens a bandgap. The bandgap frequency sensitively depends on the stripe width.

If the bilayer region width is extended to more than 25 µm, the spin-wave propagating with short wavelength decays before it reaches the detection antenna. Hence, non-reciprocity for a large frequency range is obtained. In the following, an analytical model is presented.

In the study by [Grünberg, 1981], the dispersion for magnetostatic surface spin-wave in a bilayer is calculated. The Ansatz for dispersion is conducted with dipolar coupling only. To understand, how bandgaps are opened by narrow stripes of CoFeB on top of YIG, this model was extended to the dipolar exchange regime. Therefore, exchange interaction within each of the layers is included. This work was done by Rasmus B. Holländer and will be further described in [Holländer et al., 2020].

Model by P.Grünberg [Grünberg, 1981]

In Figure 3.9, the structure to model the bilayer is displayed. Similar to [Grünberg, 1981], the structure is based on two layers of magnetic material with thickness d_A and d_B, that form a non-magnetic gap with constant distance d_0. The layers are located in x-y-plane, the spin-wave propagates parallel to y-direction, and the magnetic bias field is applied along x-direction. According to the calculation performed in [Damon and Eshbach, 1961], two solutions for spin-waves are found in one layer. In the work of [Grünberg, 1981], four solutions are found in two

magnetostatically coupled layers.
These solutions are approximated as plane waves. The Ansatz with continuity at the interfaces is:

$$\Psi_{\mathrm{in,out}} = \xi_{\mathrm{in,out}} \cdot \mathrm{e}^{i k_y y} \tag{3.2}$$

$\Psi_{\mathrm{in,out}}$ refers to the potentials **in**side or **out**side of the four layer interfaces. Furthermore, for as narrow layers as used in this work, Grünberg's publication has to be extended. The included exchange interaction is limited to *intra*layer, i.e., there is no *inter*layer exchange interaction. This is realized by the 4 nm thick spacing layer of TaOx.

Extension to Diplolar-Exchange-Range

Starting similar as [Grünberg, 1981] with the Ansatz in equation 3.2, an extended dispersion of diplolar-exchange spin-waves in the bilayer is derrived with:

$$\xi_{\mathrm{out}}(z) = \begin{cases} C \cdot \mathrm{e}^{-k_z z} & \text{if } z > \frac{d_0}{2} + d_A \\ D \cdot \mathrm{e}^{k_z z} & \text{if } z < \frac{-d_0}{2} - d_B \\ E \cdot \mathrm{e}^{k_z z} + F \cdot \mathrm{e}^{-k_z z} & \text{if } \frac{-d_0}{2} < z < \frac{d_0}{2} \end{cases} \tag{3.3}$$

$$\xi_{\mathrm{in}}(z) = \begin{cases} G_1 \cdot \mathrm{e}^{k_z z} + H_1 \cdot \mathrm{e}^{-k_z z} & \text{if } \frac{d_0}{2} < z < \frac{d_0}{2} + d_A \\ G_2 \cdot \mathrm{e}^{k_z z} + H_2 \cdot \mathrm{e}^{-k_z z} & \text{if } -\frac{-d_0}{2} - d_B < z < \frac{d_0}{2} \end{cases} \tag{3.4}$$

At the boundaries, it follows that:

$$\Psi_{\mathrm{in}}(x, z) = \Psi_{\mathrm{out}} \tag{3.5}$$

and

$$(1 + \kappa_m) \frac{\partial \Psi_{\mathrm{in}}}{\partial z} - i\nu_m \frac{\partial \Psi_{\mathrm{in}}}{\partial y} = \frac{\partial \Psi_{\mathrm{out}}}{\partial z} \quad \text{with layer index } m = A, B. \tag{3.6}$$

Here, γ is the gyromagnetic ratio and μ_0 the permeability in vacuum. $M_{\mathrm{Sat\ A,B}}$ corresponds to the saturation magnetisation of layer A or B, specifically YIG and CoFeB. $\kappa = \frac{\Omega_{\mathrm{Hm}}}{(\Omega_{\mathrm{Hm}}^2 - \Omega_m^2)}$ and $\nu = \frac{\Omega_m}{(\Omega_{\mathrm{Hm}}^2 - \Omega_m^2)}$, where $\Omega_m = \frac{\omega}{\gamma \mu_{M_{\mathrm{Sat\ A,B}}}}$ and $\Omega_{\mathrm{Hm}} = \frac{H}{M_{\mathrm{Sat\ A,B}}}$. At this point the substitution for H is made in similar fashion as on page 141 in [Stancil and Prabhakar, 2009]:

$$H \rightarrow H_{\mathrm{applied}} + \frac{2 \cdot \mathcal{A}_{\mathrm{ex.\ A,B}}}{\mu_0 M_{\mathrm{Sat\ A,B}}} \cdot k_z^2 \tag{3.7}$$

That extension consists of saturation magnetization $M_{\mathrm{Sat\ A,B}}$ in the respective layer, exchange stiffness $\mathcal{A}_{\mathrm{ex.\ A,B}}$ inside the corresponding material and wavenumber k_z in out-of-plane direction. Other than in [Grünberg, 1981], here many mixed terms arise, which do not cancel each other out. This makes the further procedure computationally complex.
When solving Equations 3.5 and 3.6 for the frequency ω, one obtains the dispersion.

The left panel of Figure 3.10 shows the dispersion relations for dipolar-exchange spin-waves in the bilayer region for different magnetic bias fields. The dispersions are calculated for 100 nm thick YIG with 50 nm thick CoFeB on top. Blue, red, and green refer to 5, 45 and 100 mT magnetic bias field. The right panel displays a comparison of the dispersion of magnetostatic surface spin-waves (yellow) to the dispersion for bilayer spin-waves (red) with a magnetic bias field of

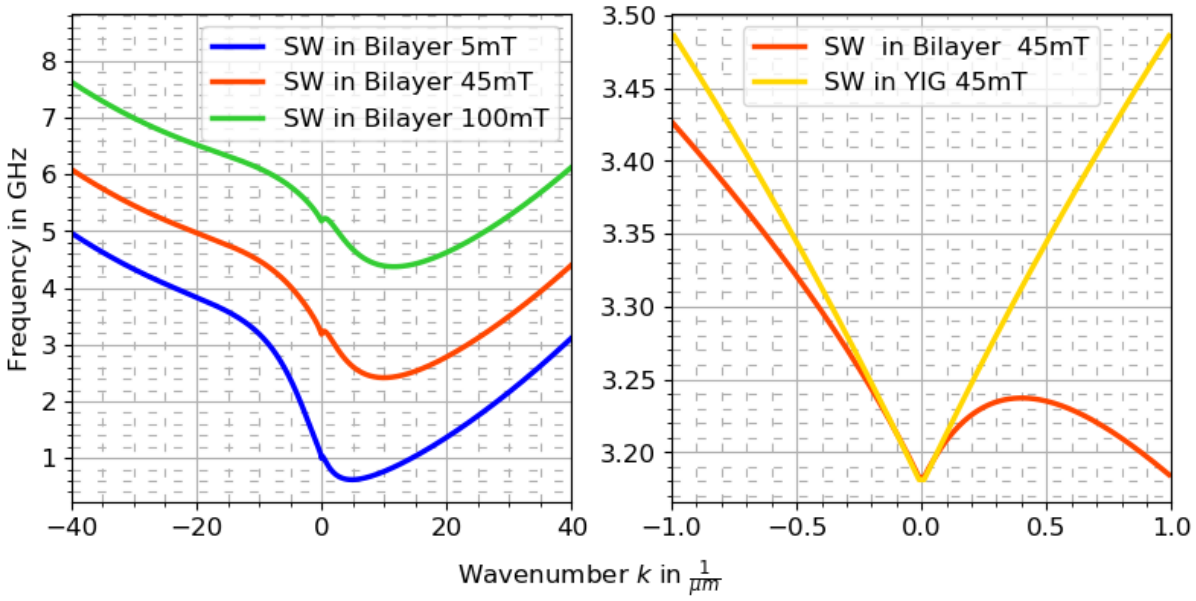

(a) (b)

Figure 3.10: Dispersion relations for YIG spin-waves in the bilayer and bare YIG areas in a magnonic resonator device. (a) Dependence of YIG-CoFeB bilayer dispersion on magnetic bias field. Blue, red, and green refer to 5, 45 and 100 mT magnetic bias field. (b) Magnified bilayer dispersion and dispersion of magnetostatic surface spin-wave in bare YIG (100 nm) for a magnetic bias field of 45 mT

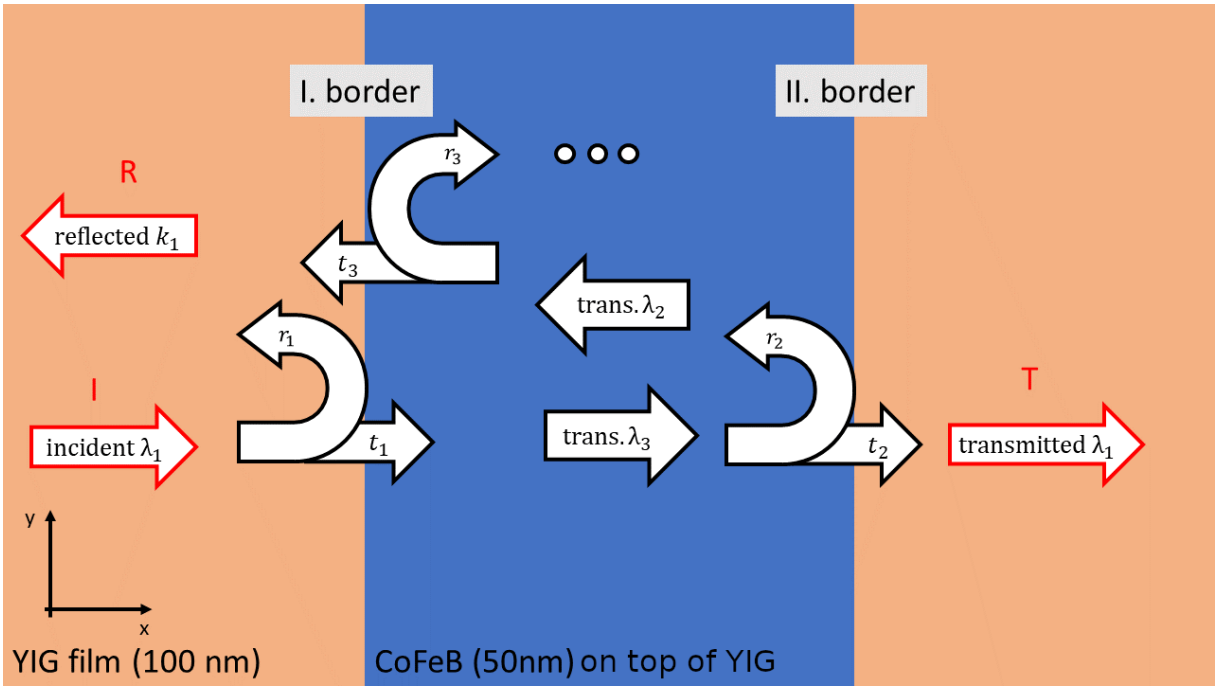

Figure 3.11: Schematic of the propagation and reflection of spin-waves in a magnonic resonator. The orange areas refer to 100 nm thick YIG. Blue corresponds to the bilayer region with 50 nm CoFeB on top of the continuous YIG. The reflection and transmission of an incoming spin-wave is depicted by white arrows.

45 mT. The FMR frequency in the bilayer is proportional to applied magnetic field strength and equal to the FMR frequency of bare YIG. For positive wavenumber, one can see that partly the dispersion has negative slope.

The new devices consist of 4 parts: (i) a continuous, non-covered YIG film, (ii) a bilayer region, where dispersion is described by the above explained model, (iii) again non-covered YIG and (iv) the exciting and detecting microwave antennas patterned on top of continuous YIG (not shown in the sketch). By using the dispersion relations shown in 3.10, the spin-wave propagation is explained as follows:
In non-covered YIG, the magnetostatic surface spin-wave propagates with the frequency f, the wave vector $\vec{k_1}$, and the wavelength λ_1. In Figure 3.11 is shown, how the spin-wave is passing the I. border of the device and transmittes into the bilayer region. There, the dispersion is altered. Thus, the magnetostatic surface spin-wave converts with positive +k while obeying energy conservation to a dipolar-exchange spin-wave with $k_{MSSW} \ll k_{DipExSW}$. Similarly, the wavelength is converted from λ_1 to $\lambda_3 \ll \lambda_1$.
For example a wave with 3.4 GHz and 45 mT applied bias field (red plot), changes from about $k_1 = 0.7\,\frac{1}{\mu m}$ to about $28\,\frac{1}{\mu m}$. Thus, the wavelength converts from $\lambda_1 = \frac{2\pi}{k} = 8.97\,\mu m$ to $\lambda_3 = 0.224\,\mu m$. When the wave now propagates to the other end of the bilayer region, it perceives a second border, at which it is again partially reflected and transmitted. The transmitted wave leaves the bilayer region and is detected at antenna 2. The reflected part, propagates back to the I. border with wavelength λ_2. It is again rereflected and according the superposition principle interferes with the unreflected wave. Analogous to Holländer, the reflection and transmission coefficients are introduced. The reflection coefficients r_I and r_{II} describe the reflection at I. and II. border. r_{III} describes the backreflection at the I. border after reflection from the II. border. The transmission coefficients t_I, t_{II}, and t_{III} are introduced in similar fashion. The transmission T through the bilayer is written as:

$$T = t_I t_{II} e^{i|k_3|\omega} \cdot \sum_{j=0}^{inf} r_{II}^j r_{III}^j \cdot e^{i\cdot j(|k_2|+|k_3|)\omega} = \frac{t_I t_{II} e^{i|k_3|\omega}}{1 - r_{II} r_{III} e^{i(|k_2|+|k_3|)\omega}} \tag{3.8}$$

By substituting $t_I t_{II} \to K \cdot e^{i\phi_I}$ and $r_{II} r_{III} \to L \cdot e^{i\phi_{II}}$, it follows:

$$\begin{aligned} T &= \frac{K \cdot e^{i(k_3\omega+\phi_I)}}{1 - L e^{i(k_2+k_3)\omega+\phi_{II}}} \\ &= \frac{K}{e^{-i(k_3\omega+\phi_I)} - L e^{ik_2\omega+\phi_{II}-\phi_I}} \end{aligned} \tag{3.9}$$

Here, k_2 and k_3 refer to wavenumbers in opposite directions within the bilayer region, while w is the width of the bilayer region. ϕ_I and ϕ_{II} corresponds to the phase jump at the I. and II. border, respectively. To predict the location of minima, transmission in equation 3.9 has to be minimized. The expression becomes minimal, when the denominator is maximal. Assuming fixed coefficients of reflection and transmission, this is fulfilled for the condition given by:

$$(|k_2| + |k_3|) \cdot w + \phi_0 = (2n + 1)\,\pi \tag{3.10}$$

$n \in \mathbb{N}$ is the order of reflection. The accumulated phase difference is the sum of phase jump at the borders and the phase difference from propagation. It is found as $\phi_0 = \phi_{prop} + \phi_{II} = 1.34\,\pi$. This is derived from micro magnetic simulations performed by Rasmus B. Holländer and Huajun Qin. This results from a more complex reflection at the magnetostatic potential well, which

changes the magnetization and, thus, dispersion and phase velocity in the border region. Also the condition depends only on ϕ_{II}. Thus, the resonance condition is determined by internal spin-wave transport, but unaffected by transmission in or out of the bilayer region The resonance condition describes destructive interference of λ_3 with wave propagating in the same direction after whole reflection cycles. When the phase difference in the denominator becomes odd multiples of π, the denominator is maximal. This condition is similar to common destructive wave interference. According to this model, the limit for this mechanism with the excitation range of the microwave antenna is 250 nm.

3.2.2 Nanoscale Magnonic Resonators

In Section 3.1 active control of spin-wave transmission by YIG-based MCs were investigated. Those devices have a size larger than nanoscale due the necessity of multiple stripes and deterioration in the YIG film induced by fabrication.
From the dispersion model for dipolar-exchange spin-wave in the section before, a new mechanism is presented that allows for active spin-wave transmission control which is achieved by a single stripe of as narrow as 250 nm stripe width. Figure 3.12 shows selected comparisons of spin-wave transmission spectra for S12 and S21 for multiple lengthscales. In Figure 3.12(a) the spin-wave transmission spectrum for bare 100 nm thick YIG is shown. By pattering a narrow CoFeB stripe of 0.7 µm width and 50 nm thickness on top of the continuous YIG (100 nm), a deep and fully reciprocal bandgap is opened in the spin-wave transmission spectra of S12 (blue) at 2.18 GHz. This leads to an efficient transmission suppression of about 83 % in the bandgap for S12 compared to bare, uncovered YIG (see Figure 3.12(a)). When a 2.5 µm wide CoFeB stripe is patterned on top of the YIG-film, two band gaps are opened in the spin-wave transmission at 1.95 GHz and 2.1 GHz. For a stripe width of 30 µm, the signal loss in S12 is almost 100 %, while the transmission in S21 amounts to about 70 % on average. Following the model in section 3.2.1, the bandgaps are opened by destructive interference. For 2.5 µm stripe width, the resonance condition in equation 3.10 is fulfilled twice within the excitation range. The totally suppressed transmission in S12 for a stripe width of 30 µm is caused by the altered damping for the converted dipolar-exchange spin-wave.

Numerically computed solution of the resonance condition in equation 3.10 and the dispersion relation predict the bandgaps reliably. In Figure 3.13(a), the measured bandgaps (crosses in blue) are compared to the calculated resonance frequency (green lines). The figure shows that for increasing widths, the bandgaps trend to higher order numbers. The order number corresponds to the phase difference equaling odd multiples of π. This is the first reported method on nanoscale to create such stable, wide and deep bandgaps in the transmission spectrum of magnetostatic surface spin-wave. Figures 3.13(b) and 3.13(c) show the tuning of transmission bandgaps opened by 0.7 µm wide stripe. By enhancing the magnetic bias field in the range of 4 mT to 50 mT, the width of that bandgap is tuned from 80 MHz to 30 MHz and the location is shifted from 1.62 GHz to 3.56 GHz.

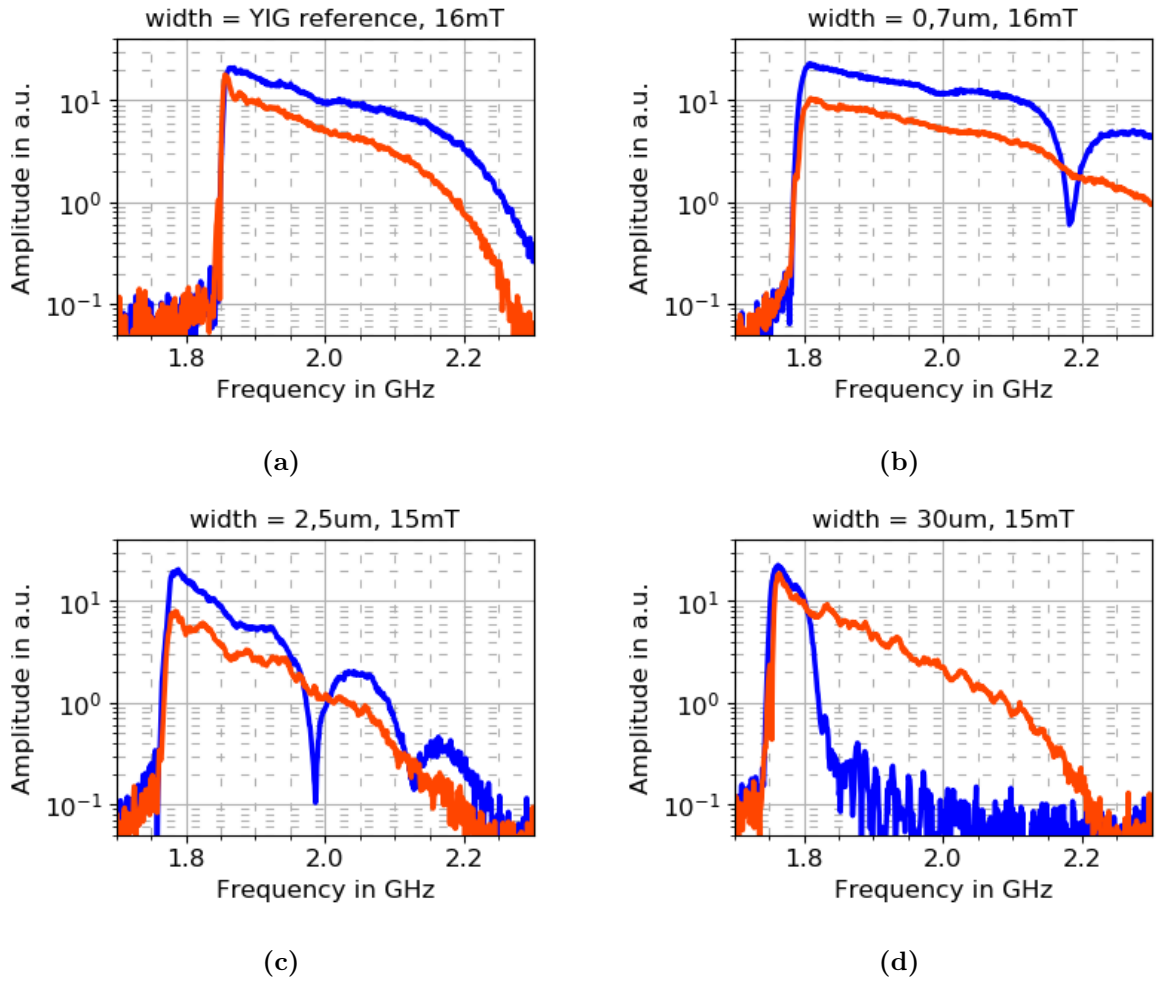

Figure 3.12: Spin-wave transmission spectra of various single magnonic resonators. The spin-wave transmission spectra for S12 (blue) and S21 (red) are compared for (a) bare YIG reference and (b) 30 µm, (c) 2.5 µm, and (d) 0.7 µm stripe width.

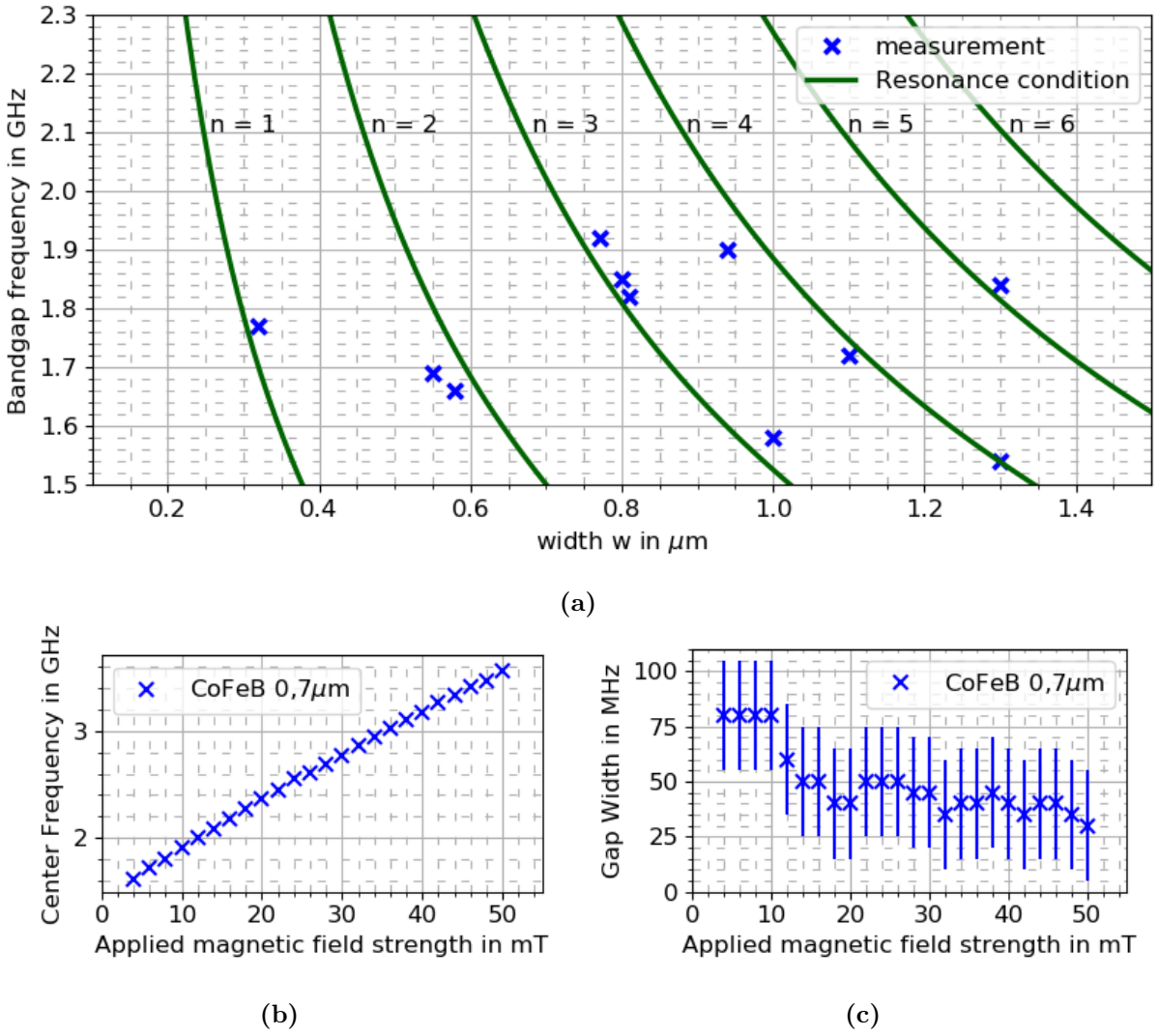

Figure 3.13: Prediction, position of the bandgap frequency, and bandgap width as a function of magnetic field and magnonic resonator width. (a), Comparison of calculated and measured magnonic resonator bandgaps for 10 mT magnetic bias field. The solid dark green lines refer numerically computed bandgap frequencies obtained from bilayer dispersion and the resonance condition 3.9. Crosses correspond to measured bandgaps. The stripe width was obtained from AFM measurements. (b), (c) show bandgap tuning for a 0.7 µm wide magnonic resonator for varying magnetic bias field.

4. Conclusion and Outlook

Using high-quality YIG film growth, direct laser writing lithography, electron-beam lithography, and magnetron sputtering, three types of magnonic devices were fabricated.
Type (i) are low loss YIG-based MCs with patterned air grooves. The devices consisted of four 12 nm deep and parallel grooves with a width ranging from 0.4 µm to 0.6 µm and a lattice period of 2 µm to 10 µm. In addition, one device with a groove depth of 18 nm was shown. By utilizing Bragg scattering, this type allows for pass band losses of only 12.5 % while suppressing spin-wave transmission by up to 99 % within the bandgaps. Varying parameters as lattice constant of the periodic stripes, stripe width or magnetic bias field strength tuned the bandgap location in a range of 1.5 GHz to 4.5 GHz and the bandgap width from 220 MHz to 50 MHz. From the MC with 18 nm groove depth, the loss of spin-wave transmission signal due to increased damping in deeply milled devices was shown.
Type (ii) is an array of magnonic resonators made from continuous YIG films with patterned CoFeB stripes on top. By avoiding milling and patterning of the YIG film, deterioration was bypassed and nanoscale device were developed.
To understand the bandgap opening mechanism and the non-reciprocity a model was introduced, explained and validated by comparison of calculations and experiments. From there a theoretical limit of 150 nm was found. A key aspect is that also single magnonic resonators (type (iii)) can be utilized. It was shown, that for narrow single stripes the bandgap location was shifted from 1.5 GHz to 3.5 GHz by changing the magnetic bias field from 4 GHz to 50 GHz and the width was tuned from 80 MHz to 30 MHz. Furthermore, for devices of type (iii) a strong non-reciprocity was observed, i.e., changing the propagation direction of spin-waves changed the transmission spectra.

By improving the microwave antenna excitation range, this mechanism could push to even smaller devices. In addition, ideas like anti-parallel switching of CoFeB stripes and YIG or multi-width arrays are to be realized. For the former, the CoFeB can be put into a remanent state with opposite magnetization as the YIG film. Simulations active reprogramming of spin-wave transmission spectra upon magnetic switching. For the latter, an array of for example 700, 750 and 800 nm wide stripes could be prepared to widen the transmission gaps. Optical control of the bandgap frequency by means of heating the metallic component on top of YIG is to be studied. Also further studies of various other material combinations or spin-wave geometries are of interest.

Outlook:

- downscaling by improving fabrication and microwave antenna excitation range
- study anti-parallel switching of magnetization for bandgaps
- investigate multiple different widths to open large bandgap structures
- use other magnetic metals in the bilayer for varying the bandgap location
- study backward volume geometry

Bibliography

[Aharoni et al., 2000] Aharoni, A. et al. (2000). *Introduction to the Theory of Ferromagnetism*, volume 109. Clarendon Press.

[Bilzer, 2007] Bilzer, C. (2007). *Microwave susceptibility of thin ferromagnetic films: metrology and insight into magnetization dynamics*. Phd thesis, Université Paris Sud - Paris XI.

[Cherepanov et al., 1993] Cherepanov, V., Kolokolov, I., and L'vov, V. (1993). The saga of yig: spectra, thermodynamics, interaction and relaxation of magnons in a complex magnet. *Physics reports*, 229(3):81–144.

[Chumak et al., 2009] Chumak, A. V., Serga, A. A., Wolff, S., Hillebrands, B., and Kostylev, M. P. (2009). Scattering of surface and volume spin waves in a magnonic crystal. *Applied Physics Letters*, 94(17):172511.

[Collet et al., 2017] Collet, M., Evelt, M., Demidov, V. E., Prieto, J. L., Muñoz, M., Youssef, J. B., de Loubens, G., Klein, O., Bortolotti, P., Cros, V., Anane, A., and Demokritov, S. O. (2017). Nano-patterned magnonic crystals based on ultrathin yig films.

[Damon and Eshbach, 1961] Damon, R. and Eshbach, J. (1961). Magnetostatic modes of a ferromagnet slab. *Journal of Physics and Chemistry of Solids*, 19(3):308 – 320.

[Daniel D. Stancil, 2009] Daniel D. Stancil, A. P. (2009). *Spin Waves; Theory and Applications*. Springer.

[Filimonov et al., 2012] Filimonov, Y., Pavlov, E., Vystostkii, S., and Nikitov, S. (2012). Magnetostatic surface wave propagation in a one-dimensional magnonic crystal with broken translational symmetry. *Applied Physics Letters*, 101(24):242408.

[Gallagher et al., 2016] Gallagher, J. C., Yang, A. S., Brangham, J. T., Esser, B. D., White, S. P., Page, M. R., Meng, K.-Y., Yu, S., Adur, R., Ruane, W., Dunsiger, S. R., McComb, D. W., Yang, F., and Hammel, P. C. (2016). Exceptionally high magnetization of stoichiometric y3fe5o12 epitaxial films grown on gd3ga5o12. *Applied Physics Letters*, 109(7):072401.

[Gilbert and Ekstein, 1956] Gilbert, T. and Ekstein, H. (1956). Basis of the domain structure variational principle. *The Bulletin of the American Physical Society*, 1:25.

[Gilbert, 2004] Gilbert, T. L. (2004). A phenomenological theory of damping in ferromagnetic materials. *IEEE Transactions on Magnetics*, 40(6):3443–3449.

[Grünberg, 1981] Grünberg, P. (1981). Magnetostatic spin wave modes of a heterogeneous ferromagnetic double layer. *Journal of Applied Physics*, 52(11):6824–6829.

[Haldar et al., 2017] Haldar, A., Tian, C., and Adeyeye, A. O. (2017). Isotropic transmission of magnon spin information without a magnetic field. *Science advances*, 3(7):e1700638.

[Hauser et al., 2016] Hauser, C., Richter, T., Homonnay, N., Eisenschmidt, C., Qaid, M., Deniz, H., Hesse, D., Sawicki, M., Ebbinghaus, S. G., and Schmidt, G. (2016). Yttrium iron garnet thin films with very low damping obtained by recrystallization of amorphous material. *Scientific reports*, 6:20827.

[Heitler and London, 1927] Heitler, W. and London, F. (1927). Wechselwirkung neutraler atome und homöopolare bindung nach der quantenmechanik. *Zeitschrift für Physik*, 44(6-7):455–472.

[Holländer, 2019] Holländer, R. B. (2019). *Dynamics of Functional Magnetic Microstructures*. PhD thesis, Universität Kiel.

[Holländer et al., 2020] Holländer, R. B., Qin, H., Hermann, F., Dreyer, R., Woltersdorf, G., and van Dijken, S. (2020). Nonreciprocal yig-based magnonic resonator for reconfigurable control of low-loss spin-wave transport, publication in preparation.

[Huber, 2013] Huber, R. (2013). *Control of Spin Waves on the Nanoscale in One-Dimensional Magnonic Crystals and Atomic Layer Deposition of Metallic Ferromagnets for Second Generation of Nanomaterials*. Dissertation, Technische Universität München, München.

[Hubert and Schäfer, 2008] Hubert, A. and Schäfer, R. (2008). *Magnetic domains: the analysis of magnetic microstructures*. Springer Science and Business Media.

[Ibach and Lüth, 2002] Ibach, H. and Lüth, H. (2002). *Solid-State Physics: An Introduction to Principles of Material Science*. Springer-Verlag.

[Kalinikos and Slavin, 1986] Kalinikos, B. A. and Slavin, A. N. (1986). Theory of dipole-exchange spin wave spectrum for ferromagnetic films with mixed exchange boundary conditions. *Journal of Physics C: Solid State Physics*, 19(35):7013–7033.

[Khitun, 2012] Khitun, A. (2012). Multi-frequency magnonic logic circuits for parallel data processing. *Journal of Applied Physics*, 111(5):054307.

[Kittel, 1948] Kittel, C. (1948). On the theory of ferromagnetic resonance absorption. *Phys. Rev.*, 73:155–161.

[Krawczyk and Grundler, 2014] Krawczyk, M. and Grundler, D. (2014). Review and prospects of magnonic crystals and devices with reprogrammable band structure. *Journal of Physics: Condensed Matter*, 26(12):123202.

[Neusser and Grundler, 2009] Neusser, S. and Grundler, D. (2009). Magnonics: Spin waves on the nanoscale. *Advanced Materials*, 21(28):2927–2932.

[Qin et al., 2018] Qin, H., Both, G.-J., Hämäläinen, S. J., Yao, L., and van Dijken, S. (2018). Low-loss yig-based magnonic crystals with large tunable bandgaps. *Nature communications*, 9(1):5445.

[Schaller, 1997] Schaller, R. R. (1997). Moore's law: past, present and future. *IEEE Spectrum*, 34(6):52–59.

["Schwarze, 2013] "Schwarze, T. (2013). *"Spin Waves in 2D and 3D Magnonic Crystals: From Nanostructured Ferromagnetic Materials to Chiral Helimagnets"*. "dissertation", "Technische Universität München", "München".

[Serga et al., 2010] Serga, A. A., Chumak, A. V., and Hillebrands, B. (2010). YIG magnonics. *Journal of Physics D: Applied Physics*, 43(26):264002.

[Serga et al., 2009] Serga, A. A., Neumann, T., Chumak, A. V., and Hillebrands, B. (2009). Generation of spin-wave pulse trains by current-controlled magnetic mirrors. *Applied Physics Letters*, 94(11):112501.

[Simons, 2004] Simons, R. (2004). *Coplanar Waveguide Circuits, Components, and Systems*. Wiley Series in Microwave and Optical Engineering. Wiley.

[Stancil, 1993] Stancil, D. D. (1993). *Theory of magnetostatic waves*. Springer-Verlag New York.

[Stancil and Prabhakar, 2009] Stancil, D. D. and Prabhakar, A. (2009). *Spin waves*, volume 5. Springer.

[Vansteenkiste et al., 2014] Vansteenkiste, A., Leliaert, J., Dvornik, M., Garcia-Sanchez, F., and Van Waeyenberge, B. (2014). The design and verification of mumax3. *AIP Advances*, 4.

[wikipedia.org, 2020] wikipedia.org (2020). Normalization (statistics).

[Wong et al., 2014] Wong, K. L., Bi, L., Bao, M., Wen, Q., Chatelon, J. P., Lin, Y.-T., Ross, C. A., Zhang, H., and Wang, K. L. (2014). Unidirectional propagation of magnetostatic surface spin waves at a magnetic film surface. *Applied Physics Letters*, 105(23):232403.

Index

LLG, 5
Damon Eshbach geometry, 7
magnetostatic surface spin-wave, 7

anisotropy , see magnetic ∼3

backward volume geometry, 8
bilayer resonator scheme, 35

dipolar coupling , see magnetostatic contr.5

exchange integral, 4
exchange interaction, 4

Fabrication, *see* Smple Preparation11
ferromagnetic resonance, 6
forward volume geometry, 8

Gilbert damping, 7
Growth, 11

Heisenberg hamiltonian, 4

Kittel-Formula, 7

Landau-Lifshitz-Gilbert Equation, 5

magnetic anisotropy, 3
Magnetism, 3
magnetostatic contribution, 5
magnonic crystal, 9
magnonic resonator, 9
MSSW , see magnetostatic surface spin-wave7

Sample Preparation, 11
Scattering Parameters, 11
spin-waves, 6

Zeeman energy, 4